A: Environmental, Combustion, and Atmospheric Chemistry; Aerosol Processes, Geochemistry, and Astrochemistry

Probing the OH Oxidation of Pinonic Acid at the Air-Water Interface Using Field-Induced Droplet Ionization Mass Spectrometry (FIDI-MS)

Yuanlong Huang, Kevin M. Barraza, Christopher M Kenseth, Ran Zhao, Chen Wang, Jesse Lee Beauchamp, and John H. Seinfeld

J. Phys. Chem. A, **Just Accepted Manuscript** • Publication Date (Web): 16 Jul 2018

Probing the OH Oxidation of Pinonic Acid at the Air-Water Interface Using Field-Induced Droplet Ionization Mass Spectrometry (FIDI-MS)

Yuanlong Huang,[†,‖] Kevin M. Barraza,[‡,‖] Christopher M. Kenseth,[‡] Ran Zhao,[‡,⊥] Chen Wang,[¶] Jesse L. Beauchamp,[‡] and John H. Seinfeld[*,‡,§]

†*Division of Geological and Planetary Sciences, California Institute of Technology, Pasadena, CA, USA, 91125*

‡*Division of Chemistry and Chemical Engineering, California Institute of Technology, Pasadena, CA, USA, 91125*

¶*Department of Chemistry and Department of Physical and Environmental Sciences, University of Toronto, Toronto, ON, Canada*

§*Division of Engineering and Applied Science, California Institute of Technology, Pasadena, CA, USA, 91125*

‖*These authors contributed equally to this work*

⊥*Now at: Department of Chemistry, University of Alberta, Edmonton, AB, Canada T6G 2G2*

E-mail: seinfeld@caltech.edu

Phone: +1 626 395 4635. Fax: +1 626 796 2591

Abstract

Gas and aqueous phases are essential media for atmospheric chemistry and aerosol formation. Numerous studies have focused on aqueous-phase reactions as well as coupled gas/aqueous-phase mass transport and reaction. Few studies have directly addressed processes occurring at the air-water interface, especially involving surface-active compounds. We report here the application of field-induced droplet ionization mass spectrometry (FIDI-MS) to chemical reactions occurring at the atmospheric air-water interface. We determine the air-water interfacial OH radical reaction rate constants for sodium dodecyl sulfate (SDS), a common surfactant, and pinonic acid (PA), a surface-active species and proxy for biogenic atmospheric oxidation products, as 2.87×10^{-8} and 9.38×10^{-8} cm^2 molec^{-1} s^{-1}, respectively. In support of the experimental data, a comprehensive gas-surface-aqueous multiphase transport and reaction model of general applicability to atmospheric interfacial processes is developed. Through application of the model, PA is shown to be oxidized exclusively at the air-water interface of droplets with a diameter of 5 μm under typical ambient OH levels. In the absence of interfacial reaction, aqueous- rather than gas-phase oxidation is the major PA sink. We demonstrate the critical importance of air-water interfacial chemistry in determining the fate of surface-active species.

Introduction

The hydroxyl radical (OH) is the fundamental oxidant in the atmosphere. In addition to reaction with gas-phase molecules (e.g., volatile organic compounds), OH reaction can modify the physico-chemical properties (e.g., surface tension, hygroscopicity, composition, etc.) of airborne particles through heterogeneous chemistry.[1] Heterogeneous OH-initiated oxidation of particles can be confined to the interface due to the particle bulk properties, such as high viscosity[2]. The air-water interface is ubiquitous in the atmosphere owing to the high surface-to-volume ratio of cloud and fog droplets. Moreover, heterogeneous reaction at the air-water

interface can be facilitated if the air-water interface lowers the reaction energy barrier.[3] In addition, organic molecules at the air-water interface may have preferred orientation as a result of hydrogen bonding involving substituent groups[4] thus the reaction mechanisms at the air-water interface can differ from those of gas- and aqueous-phase reactions.[5–11] Studies of the air-water interfacial oxidation of organic compounds have been focused on the effects of substitutions,[12] unsaturation,[13,14] and chain length[15] on reaction kinetics and mechanisms.

Pinonic acid (PA) is a major oxidation product of α-pinene, one of the most abundant biogenic volatile organic compounds emitted to the atmosphere (global emissions estimated at 66.1 Tg/y).[16] Studies have focused on gas- and aqueous-phase oxidation of PA by OH.[17,18] Upon oxidation by OH, PA has been shown to have a high potential to form the secondary organic aerosols (SOA).[19,20] With a saturation vapor pressure of $\sim 7 \times 10^{-5}$ Pa at 296 K,[21] PA partitions between the gas and particle phases. Given its high Henry's law constant of $\sim 2 \times 10^{7}$ M atm^{-1},[22] PA tends to reside in the aqueous phase under cloudy and foggy conditions, or in the presence of aerosol liquid water. Although PA has been shown to be a highly surface-active species in the atmosphere,[23] limited studies have been directed to its behavior at the air-water interface.[8,24] Enami and Sakamoto[24] showed that PA resides at the air-water interface and observed peroxyl radicals and hydroperoxides at the early stage of exposure of PA solution droplets to OH. Though OH oxidation of PA at the air-water interface is rapid, kinetic data of the interfacial reaction have been lacking. Lai et al.[25] estimated the atmospheric lifetime of PA as 2.1 - 3.3 days under environmentally relevant humidity conditions based on heterogeneous OH oxidation of PA film as opposed to an actual air-water interface. Given its high surface activity and tendency to partition to the aqueous phase, investigation of mechanisms and kinetics of interfacial oxidation of PA by OH under atmospheric conditions is addressed here.

We employ field-induced droplet ionization mass spectrometry (FIDI-MS) to investigate the OH oxidation of pinonic acid at the air-water interface.[26,27] FIDI-MS is differentiated from other mass spectrometric techniques by the ability to perform online detection of chem-

ical species at the air-water interface via a surface-selective sampling mechanism, for which the ionization process has been studied extensively. The FIDI sampling apparatus produces millimeter-sized water droplets containing analytes at concentrations relevant to the ambient atmosphere (i.e., clouds, fog, and aerosol liquid water). Because of the specificity of sampling, FIDI-MS has been employed to monitor the adsorption and heterogeneous chemistry of organic compounds at the air-water interface of both atmospherically[28–30] and biologically[31–33] relevant systems. The controllable time scale for reaction in FIDI-MS makes it possible to track the kinetics of interfacial reactions over many half-lives and multiple generations of oxidation.

Through study of the OH oxidation of PA at the air-water interface with FIDI-MS, we seek to elucidate the mechanistic details of its surface reaction. To interpret the kinetic data, we develop a gas-surface-aqueous multiphase transport and reaction model that describes the heterogeneous OH oxidation of PA and constrains the surface reaction rate constant of PA + OH at the air-water interface. For the first time, the interplay between chemistry, diffusion, and phase-partitioning occurring at a droplet's air-water interface is investigated. We demonstrate that under typical ambient OH levels ($\sim 10^6$ molec cm^{-3}), the majority of the multiphase PA oxidation occurs on the surface of water droplets representative of cloud/fog water. In short, the present study addresses the importance of interfacial oxidation for surface-active atmospheric species.

Methods

Experimental Setup

A schematic diagram of the FIDI-MS setup is depicted in Figure 1; a detailed description of the FIDI-MS method is presented elsewhere.[26,27] Briefly, an aqueous droplet of $\sim$2 mm diameter (~ 4 μL volume) is suspended on the end of a stainless steel capillary held equidistant between two parallel plate electrodes separated by 6.3 mm (Fig. 1a). Droplets are

formed from analyte solutions fed through the capillary using a motorized syringe pump. The parallel plates are mounted on a translation stage to allow alignment of an aperture in the electrically grounded front plate with the atmospheric pressure inlet of an LTQ-XL mass spectrometer (Thermo-Fischer, Waltham, MA) that is open to ambient lab air. Following droplet formation, a period of 60 s is allowed for diffusion of surface-active species to achieve equilibrium coverage at the air-water interface. The sampling of the hanging droplet proceeds by applying a high voltage pulse (3 - 5 kV, 100 ms duration, variable polarity) to the back plate electrode and to the capillary at half the magnitude supplied to the back plate, establishing a homogeneous electric field. The electric field induces an aligned dipole that stretches the suspended droplet until dual Taylor cones are formed at opposite ends, ejecting charged sub-micrometer progeny droplets of opposite polarity toward the appropriately biased electrodes (Fig. 1b). Progeny droplets of a specific polarity pass through the aperture in the grounded front plate and enter the inlet of the mass spectrometer, resulting in the detection of gas-phase ions. As FIDI sampling causes significant perturbation to the droplet, a fresh droplet is generated for each measurement. In many respects, the FIDI process is similar to that of electrospray ionization (ESI), except that sampling occurs only from the sheared electrical double layer at the droplet surface. In this study, a negative voltage was applied to the back plate and capillary to detect deprotonated $[M-H]^-$ ions.

A dielectric barrier discharge source (DBDS) was used to generated hydroxyl radicals. The DBDS consists of a 38 mm borosilicate tube (6.45 mm O.D., 3.91 mm I.D.) with a tungsten rod (1.02 mm diameter) inner electrode and a conductive silver epoxy outer electrode. A bubbler provides water-saturated helium through the DBDS with flow monitored by a Type πMFC digital mass flow controller (model PFC-50, MKS Instruments). A high voltage AC power supply (Trek PM04015, Trek, Inc) biases the inner electrode during experiments, while the outer electrode remains grounded. The operational conditions of the DBDS are as follows: 12 kVpp (peak-to-peak AC voltage) bias, 1 kHz sine waveform, 1.414 mA current, and 1000 cm^3 min^{-1} He/H_2O flow. The proposed mechanism of OH generation proceeds either

directly via an electron capture reaction with water ($e^- + H_2O \longrightarrow H^- + OH$), or through a two-step process ($e^- + H_2O \longrightarrow H_2O^+ + 2\,e^-$ and $H_2O^+ + H_2O \longrightarrow H_3O^+ + OH$).[34] No H, O, or HO_2 is anticipated to form in the DBDS. The characterization of gas-phase OH concentration will be discussed subsequently.

Ultra-pure water (18 MΩ, < 3 ppb TOC, Millipore Milli-Q) and HPLC grade methanol (J.T.Baker) were used as solvents. Aqueous stock solutions of *cis*-pinonic acid (PA, 98%, Sigma-Aldrich) and sodium dodecyl sulfate (SDS, 98%, Fischer Scientific) were prepared at concentrations of 5 mM and 2 mM, respectively, and diluted as needed. Settings for FIDI-MS were optimized for deprotonated *cis*-pinonic acid $[PA-H]^-$ using a 20 μM solution of PA in 99.2:0.8 methanol:water (v/v%).

To study the interfacial OH + PA reaction mechanism, an aqueous PA droplet with an average bulk concentration of 50 μM is exposed to OH from the DBDS for varying reaction times, at which concentration, based on its equilibrium constant, ∼19% of PA is estimated to remain on the surface of the droplet with a radius of 1 mm. Droplets of 20 μM SDS were exposed to the OH source for different durations to characterize the gas-phase OH concentration. To constrain the surface reaction rate constant for OH + PA, a mixture of PA and SDS solution is diluted to 50 and 20 μM, respectively. Under each reaction condition, 5 droplets were repeated and averaged to overcome drop-to-drop variation.

Diffusion-Reaction Interfacial Model

We present the development of a diffusion-reaction model designed to describe the air-water interfacial reaction on a droplet between gas-phase OH and a surface-active component, PA in this study. In addition to its surface reaction with OH, PA can evaporate into the gas phase, diffuse into the bulk droplet, and undergo bulk oxidation if dissolved OH is present. Sodium dodecyl sulfate (SDS) is used as a reference compound that, in contrast to PA, given its high molecular weight and long alkyl chain, undergoes only surface reaction, i.e., no evaporation and no diffusion into the bulk. Moreover, SDS oxidation products are easy

to characterize at early timescales as SDS undergoes sequential oxygenation with negligible fragmentation. As such, by measuring the rate of decay of SDS on the surface, one can infer the gas-phase OH concentration, and, in turn, calculate the surface reaction rate constant with OH for the surface active species. The model accounts for each of these transport and reaction processes explicitly, for both PA and SDS, in order to extract the surface reaction rate of PA + OH from the experimental data.

The physical system to which this model is applied is depicted in Fig. 2; additional details of the model are discussed in Supporting Information SI.I. The following reactions describe the transport and reaction processes:

$$\mathrm{OH}(gs) \rightleftharpoons \mathrm{OH}(s) \tag{R 1}$$

$$\mathrm{PA}(gs) \rightleftharpoons \mathrm{PA}(s) \tag{R 2}$$

$$\mathrm{PA}_p(gs) \rightleftharpoons \mathrm{PA}_p(s) \tag{R 3}$$

$$\mathrm{OH}(s) + \mathrm{SDS}(s) \longrightarrow \mathrm{SDS}_{p1}(s) \xrightarrow{\mathrm{OH}(s)} \mathrm{SDS}_{p2}(s) \xrightarrow{\mathrm{OH}(s)} \mathrm{SDS}_{p3}(s) \xrightarrow{\mathrm{OH}(s)} \ldots \tag{R 4}$$

$$\mathrm{OH}(s) + \mathrm{PA}(s) \longrightarrow \mathrm{PA}_p(s) \tag{R 5}$$

$$\mathrm{OH}(s) \rightleftharpoons \mathrm{OH}(b) \tag{R 6}$$

$$\mathrm{PA}(s) \rightleftharpoons \mathrm{PA}(b) \tag{R 7}$$

$$\mathrm{PA}_p(s) \rightleftharpoons \mathrm{PA}_p(b) \tag{R 8}$$

$$\mathrm{OH}(b) + \mathrm{PA}(b) \longrightarrow \mathrm{PA}_p(b) \tag{R 9}$$

where s refers to the surface, b represents the bulk aqueous phase, and gs denotes the gas phase within one molecular mean free path above the surface. Note that gs is distinct from g, the bulk gas phase sufficiently far from the surface. Differences in concentrations between gs and g is described in SI.I.

R1, R2, and R3 correspond to the surface adsorption and desorption of OH, PA, and PA products (PA_p), respectively. R4 and R5 are the surface reaction of SDS + OH and PA + OH. R6, R7, and R8 represent surface to bulk droplet transport. R9 represents the bulk aqueous-phase reaction of PA + OH. The forward and reverse reaction rate constants for R1 - R3 and R6 - R8 follow the multi-phase transport theory in Pöschl et al.[35] and are explicitly discussed in SI.I. The bulk aqueous-phase rate constant of PA + OH in R9 is adopted from Aljawhary et al.[20]. R4 and R5 are the key processes on which we focus here. Values of key parameters are summarized in Table 1.

The gas-phase OH concentration sufficiently far from the droplet surface is assumed to be constant, based on the assumption that the OH concentration from the DBDS is constant. Close to the droplet, however, a concentration gradient exists that depends on the OH uptake coefficient (γ_{gs}). During the reaction period, the droplet size is assumed to be constant, i.e., no water evaporation occurs. However, evaporation of surface-active PA is considered (R2). The Langmuir adsorption model (monolayer) is used to calculate the initial surface coverage of PA given the bulk concentration of the PA solution from which the droplet is formed (See SI.II). When PA and SDS coexist in the droplet, we assume that PA and SDS do not interact, that the surface coverages of PA and SDS are equivalent (i.e., $\theta_{0,PA} = \theta_{0,SDS} = 1$), and that the surface coverage is homogeneous. An implicit assumption is the absence of reaction between PA, SDS, and their products.

OH surface reactions are assumed to follow Langmuir-Hinshelwood kinetics,[35,36] i.e., OH first adsorbs to the organic surface (R1) and then reacts interfacially with PA and SDS (R4 and R5). This assumption is consistent with the experimental data, as will be discussed subsequently. The adsorption property of OH is following Vácha et al.[37]. Adsorbed OH can also diffuse into the droplet (R6) and react with PA in the bulk aqueous phase (R9).[38] The oxidation products of SDS + OH are assumed to stay in the interface, since even after several generations of oxidation the long alkyl chain remains largely intact (i.e., functionalization predominates). The SDS oxidation products are assumed to continue to react with adsorbed

OH at different rates (R4). For simplicity, the first-generation oxidation products of the PA + OH reactions at the interface (R5) and in the bulk (R9) are represented as single lumped products, $PA_p(s)$ and $PA_p(b)$. $PA_p(s)$ and $PA_p(b)$ are assumed to have equivalent compositions and properties, even though their formation rates and mechanisms may differ. Depletion of the PA(s) by reaction with OH is replenished by aqueous-phase diffusion of $PA_p(b)$ toward the surface (R7). Equilibrium partitioning of PA and PA_p between the gas phase, the surface and the aqueous phase was estimated using the quantum chemical program COSMOtherm based on density functional theory calculations (see SI.III for details).[39,40] The predicted surface/water and surface/air equilibrium constants for PA and proposed products of the interfacial reaction of PA + OH (see Results and Discussion) are listed in Table S1. The predicted equilibrium constants for the PA oxidation products span several orders of magnitude. For simplicity, the lumped PA oxidation product PA_p is assumed to have the same equilibrium constants as PA. Subsequent reactions of the lumped PA products, PA_p, with OH are also represented in the model.

Results and Discussion

OH Oxidation of Pinonic Acid Droplet

As a compound of intermediate volatility,[40] we first examine the extent to which PA evaporates from the droplet. Both experimental and simulation results (SI.IV) suggest that changes in PA concentration due to evaporation within the experimental timescale of 100 s are negligible. Figure 3 depicts the mass spectra of a PA droplet, in 10 s intervals, over a 30 s OH exposure. A series of six major oxidation products, at m/z 197 (I), 199 (II), 213 (III), 215 (IV), 229 (V), and 231 (VI) are identified. Since FIDI-MS provides only unit-mass resolution, each peak likely represents the combination of several isomers and isobars. As a first approximation, $[PA-H]^-+14$ is assumed to represent the addition of one carbonyl (>C=O), $[PA-H]^-+16$ the addition of one hydroxyl (-OH), $[PA-H]^-+30$ the addition of

one carboxylic acid (-C(=O)OH) or one hydroxyl and one carbonyl, and $[M-H]^-+32$ the addition of two hydroxyls or one hydroperoxyl (-OOH).

As shown in Fig. 4, the initial H-abstraction by OH from PA can occur at 7 possible sites (a - g). Quantum chemical calculations suggest that in gas-phase OH oxidation, H-abstraction occurs most likely on carbon f.[17,41] However, results of structure activity relationships (SAR) for OH oxidation in the aqueous-phase indicate that carbons a and c are preferred positions.[18] At the air-water interface, molecular dynamics simulations[23] suggest that PA molecules are oriented such that the hydrophilic functional groups (-C(=O)OH and >C=O) are embedded in the droplet, while the hydrophobic cyclobutyl ring is exposed on the droplet surface (see Fig. 2), making carbons a-c the most vulnerable to OH attack. Following the initial H-abstraction (Fig. 4), the resulting alkyl radical combines exclusively with O_2 at the air-water interface to form a peroxyl radical (RO_2), which may undergo the same competitive reaction channels as those in the gas phase.[42] The three dominant gas-phase bimolecular reactions are $RO_2 + RO_2$ ($k_{RO2} \sim 10^{-14} - 10^{-12}$ cm^3 molec^{-1} s^{-1}), $RO_2 +$ NO ($k_{NO} = 7 - 10 \times 10^{-12}$ cm^3 molec^{-1} s^{-1}), and $RO_2 + HO_2$ ($k_{HO_2} = 5 - 20 \times 10^{-12}$ cm^3 molec^{-1} s^{-1}).[42,43] Note that the aqueous-phase $RO_2 + RO_2$ and $RO_2 + HO_2$ reactions have similar rate constants (10^9 M^{-1} s^{-1} $\sim 1.7 \times 10^{-12}$ molecule^{-1} cm^3 s^{-1})[44,45] as those in the gas-phase. Assuming NO and HO_2 have similar air-water interfacial adsorptive and reactive properties, and given that the FIDI source is exposed to the ambient atmosphere and typical daily average NO mixing ratio in the Los Angeles area is $\sim$ 1 ppb ($10^{11} - 10^{12}$ molec cm^{-3})[46,47] and indoor HO_2 mixing ratio $<$ 10 ppt ($\sim 10^9$ molec cm^{-3}),[48] it is expected that reaction with NO is the dominant fate of PA peroxyl radicals at the air-water interface, with a small fraction of $RO_2 + RO_2$ and $RO_2 + HO_2$ reactions (Fig. 4). Reaction of $RO_2 +$ NO yields alkoxy radicals (RO) that undergo decomposition, isomerization, or reaction with O_2.[49]

To aid in identification of the compounds that contribute to the six major mass spectral peaks detected by FIDI-MS, collision-induced dissociation (CID) was employed for detailed

analysis of molecular structure. The MS/MS fragmentation patterns of the six parent ions are shown in Fig. S5. The daughter ions in each MS/MS spectrum can be explained by neutral losses of H_2O, CO_2, C_3H_6O, and $C_6H_{10}O$ [50] (Fig. S5). Certain neutral losses are characteristic to specific functional groups, e.g., carboxylic acid ions exhibit losses of 18 u (H_2O) and 44 u (CO_2).[51] All structures proposed in Fig. 4 are consistent with the observed MS/MS spectra. The peak at m/z 197 can be explained by a $C_{10}H_{14}O_4$ species derived from the RO_2 formed by H-abstraction from carbon a via successive reactions with NO and O_2 or through Russell disproportionation[52]. The compound at m/z 199 can also form through the Russell mechanism. The RO formed through OH-attack on carbon a can undergo ring-opening processes via scission of either the a-b or a-c bonds (for simplification, Fig. 4 depicts only the cleavage of the a-c bond), yielding a new alkyl radical, which after reacting with O_2 and NO forms another RO. This intermediate RO can undergo 1,5 H-shift to form the species at m/z 229 and m/z 231, react with O_2 to yield m/z 213, or react with RO to yield what is believed to be a minor product at m/z 215. H-abstraction from carbons b or c leads to the formation of a RO, which will decompose, react with O_2 and NO, and ultimately yield a tertiary RO. The resulting tertiary alcohol at m/z 215 shown in Fig. 4 is expected to be the major isobaric contributor at this m/z, given its agreement with the major fragments observed in the MS/MS spectrum.

The aqueous-phase pH can affect the reaction mechanism as well as the reaction rate.[18] Given $pK_a = 4.82$,[53] the pH in the bulk droplet of PA solution at equilibrium with the surface is at most 5.2 and the ratio of deprotonated PA to PA is ~ 2.2 (assuming the surface and the bulk are decoupled). Deprotonated PA has an additional reaction pathway in the aqueous phase, i.e., electron transfer.[54] However, the undissociated PA is expected to dominate at the surface.[55] Thus Fig. 4 only illustrates the mechanism of undissociated PA reacted with OH at the air-water interface.

The kinetic behavior of PA and its 6 oxidation products is shown in Fig. S6. The relative rates of appearance of each product are consistent with the PA reaction pathways proposed

based on MS/MS analysis. While I and II are both the lowest mass products, the considerably slower rate of appearance of II suggests that this product is formed by a slower and/or more complex mechanism. Fig. 4 proposes a fragmentation product (H-abstraction from carbons d or e) as one of the possible structures of II, whereas I is suggested to be predominantly due to functionalization. The highest mass species (V and VI) are characterized by the highest level of oxidation. The kinetic behavior of V and VI indicates a net balance between formation and degradation pathways for these species, suggesting that as the O/C ratio increases, the interfacial OH + PA oxidation system exhibits a propensity to shift from functionalization to fragmentation products.

Characterization of Gas-Phase OH Concentration

To study the kinetics of interfacial OH oxidation of PA, a sufficient constraint on the gas-phase OH concentration is necessary. By monitoring the heterogeneous OH oxidation of surfactant, i.e., SDS in this study, and assuming that the surfactant remains exclusively on the surface, one can infer the gas-phase OH concentration. As stated in the Model description section, it is necessary to incorporate all possible processes, i.e., adsorption and reaction on the surface, as well as diffusion in the bulk droplet, into a unified model, from which the gas-phase OH concentration can be inferred.

Assuming an effective cross-section area of 30 $Å^2$ for SDS[56] and that the SDS resides solely at the surface, a monolayer of SDS is formed on the surface of a droplet with a radius of 1 mm. Mass spectra of the interfacial OH oxidation of SDS are shown in Fig. S7, and the measured decay of SDS is shown in Fig. 5a. Due to the linear alkyl chain, the successive increases of m/z 14 and 16 indicate that alcohols and carbonyls are the most likely products via RO_2 / RO chemistry in the SDS + OH reaction. However, other functionalities, e.g., carboxylic acids ($m/z + 30$), are possible. Instead of assigning specific formula to each m/z peak, the products can be clustered into groups, i.e., peaks at m/z $[DS]^- + 14$ and $[DS]^- + 16$ are grouped into the products that contain one oxygen atom, while products at m/z $[DS]^-$ +

28, $[DS]^- + 30$, and $[DS]^- + 32$ are those with two oxygen atoms, etc. Figure 5b presents the temporal profiles of 8 generations of identified SDS + OH oxidation products. Assuming that SDS incorporates one oxygen after reacting with one OH, by defining the average oxygen atom as the signal-intensity-weighted sum of the oxygen content in the identified oxidation products (m/z 265 - 400), the experimental results indicate that ∼10 s is required for OH to react with the entire monolayer of SDS (Fig. 5c). The near-linear relationship in Fig. 5c suggests Langmuir-Hinshelwood kinetics govern the air-water system, since if OH were to react with the interfacial molecules upon collision (Eley-Rideal mechanism) the rate of oxygen atom incorporation would increase as the reaction progresses given that more reactive C-H bonds are formed, e.g., those adjacent to a carbonyl group.

By fitting the experimental data in Fig. 5a-c, we seek to estimate the gas-phase OH concentration, as well as the surface reaction rate constants for both SDS and SDS products. The best-fit gas-phase OH mixing ratio is found to be ∼698 ppb. The experimental distribution patterns of the eight oxidation generations and the decay curve of SDS determine the reaction rate constants of $SDS_p + OH$ to relative that of SDS + OH, i.e., $k_{\text{surf}}^{\text{OH+SDS}}$. All generations are found to react faster with OH than SDS. Nonetheless, without any constraint on the surface concentration of OH, the optimally fitted $k_{\text{surf}}^{\text{OH+SDS}}$ values span from 10^{-11} to 10^{-4} cm^2 molec^{-1} s^{-1}, within which range, $k_{\text{surf}}^{\text{OH+SDS}}\theta_{\text{OH}}$ (Fig. S8a) is nearly constant, suggesting that the decay of SDS is a quasi-first-order reaction (∼0.0516 s^{-1}). Figure 5d shows the estimated average OH uptake coefficient γ_{gs} and the gas-phase OH concentration above the surface C_{gs}^{OH} as functions of the optimally fitted $k_{\text{surf}}^{\text{OH+SDS}}$. In the regime where $k_{\text{surf}}^{\text{OH+SDS}} > 10^{-7}$ cm^2 molec^{-1} s^{-1}, both γ_{gs} and C_{gs}^{OH} remain constant, which is a result of the fast surface reaction rate causing gas-phase diffusion of OH to the surface to become the rate-limiting step in this system. γ_{gs} of OH onto thin organic film is typically ≥ 0.1[1] and the gas-phase diffusion limit is unlikely in the FIDI experiment since the DBDS aims directly at the droplet. Adopting a median value $\gamma_{gs} = 0.5$, we find the average values $C_{gs}^{OH} \approx 6 \times 10^9$ molec cm^{-3}, $k_{\text{surf}}^{\text{OH+SDS}} \approx 2.87 \times 10^{-8}$ cm^2 molec^{-1} s^{-1}, and $\theta_{\text{OH}} \approx 10^{-9}$. Figure 5a and c show

the calculated temporal profiles of C_{gs}^{OH} and γ_{gs}.

The simulation suggests that in the absence of bulk reaction consuming aqueous-phase OH, OH radicals can diffuse to the center of the droplet and reach ~1 nM after 30 s (Fig. S8b), indicating that the bulk droplet serves as a significant sink of OH in the OH + SDS interfacial reaction system. The high gas-phase OH concentration above the surface gives $\sim 10^{11}$ molec cm^{-3} s OH exposure in the FIDI system, corresponding to $\sim$ 1 day exposure under typical atmospheric conditions (assuming ambient OH concentration of 1×10^6 molec cm^{-3}). The air-interface-water properties of OH employed in the model and the best-fit surface reaction rate constant of SDS + OH are summarized in Table 1.

Kinetics of Interfacial OH Oxidation of Pinonic Acid

PA partitions between the droplet surface and bulk. Because of diffusion to the bulk of both PA and PA oxidation products, one can not use the same strategy as employed for OH + SDS to determine the surface reaction rate constant. As discussed above, the products of PA + OH are complex, and it is impossible to track the fractions of all the PA products that diffuse into the bulk. By adding a reference compound to the system, such as a surfactant that undergoes only surface reaction, we can better constrain the OH concentration on the surface and determine the surface reaction rate constant for OH + PA. The resulting mass spectra under different exposure times are shown in Fig. 6a. The decay of both PA and SDS is shown in Fig. 6b. The apparent decay rate of PA exceeds that of SDS, which is indicative of the relative reactivity of PA. One cannot, however, rule out the possibility that bulk aqueous-phase transport and oxidation can affect the decay rate.

By fitting to the data points in Fig. 6b, where the surface reaction rate constants for both SDS and SDS products are known, the bulk gas-phase OH concentration is estimated as ~678 ppb, consistent with the value evaluated for SDS + OH experiments, demonstrating the reproducibility of DBDS employed for air-water interfacial oxidation studies. The surface reaction rate constant of PA + OH is determined to be 9.38×10^{-8} cm^2 molec^{-1} s^{-1}, ~3

times of that of SDS + OH. The fitted surface rate constant of PA + OH is not sensitive to the surface coverage of PA and SDS. The gas-phase OH concentration above the surface is $\sim 5 \times 10^9$ molec cm^{-3} and the OH uptake coefficient is ~0.35 (Fig. 6c).

The calculated average oxygen atom incorporation into SDS products fits the experimental data (Fig. S9a) as well. The simulated bulk aqueous-phase OH distribution (Fig. 6d) predicts that OH is confined to the surface region (within a distance of ~1 μm). The heterogeneous nature of the reactions can be quantified by utilizing the concept of a reacto-diffusive length L_{OH}:[35]

$$L_{OH} = \sqrt{\frac{\mathcal{D}_b^{OH}}{k_b^{OH+PA} C_b^{PA}}} \quad (1)$$

where $\mathcal{D}_b^{OH}$ is the bulk diffusion coefficient of OH (2.3×10^{-9} m^2 s^{-1}), k_b^{OH+PA} is the bulk reaction rate constant of PA + OH (3.3×10^9 M^{-1} s^{-1}),[20] and C_b^{PA} is the bulk concentration of PA ($\sim(1 - 19\%) \times 50$ μM). In this system, $L_{OH} \approx 0.6$ μm, consistent with the prediction of the simulation (Fig. 6d). To replenish its consumption by OH in the sub-surface region, a continuous diffusive flux of PA from the bulk aqueous phase has to be established (Fig. S9b). Though the surface reaction rate constant of PA + OH is faster than that of SDS + OH, the simulated decay curves of PA and SDS cross after 30 s exposure to OH, since at that point replenishment of PA from the bulk competes with the surface reaction rate.

In summary, to determine the air-water interfacial reaction rate constant of a surface-active species, one has to account for simultaneous aqueous-phase diffusion and reaction. For a system with high bulk OH reactivity ($k_b^{II} C_b$, where k_b^{II} is a second-order aqueous-phase reaction rate constant and C_b is the bulk aqueous-phase concentration of the surface-active species), the heterogeneous reaction is enhanced, since the penetration of OH into the droplet bulk is confined to the sub-surface region. If the bulk reaction rate is smaller than that on the surface, a slower "apparent" decay rate of the surface coverage can be expected due to the replenishment from bulk diffusion.

Atmospheric Implications

In the atmosphere in which cloud and fog droplets or aerosol water are present, for species with high Henry's law constants, a large fraction will partition to the aqueous phase, where aqueous phase chemistry can be significant.[57–59] The Henry's law constant relates the gas and bulk aqueous phases and is routinely adopted in the cloud or aqueous aerosol chemistry models.[60,61] However, by accounting for the surface activity, the fraction that partitions in the gas phase, on the surface, and in the bulk aqueous phase may be quite different. The fraction partitioning on the surface of the droplet, F_{surf}, can be estimated by

$$F_{\mathrm{surf}} = \frac{\frac{3w_L}{\overline{R_p}}}{\frac{1}{\mathrm{K}_{sg}} + \frac{w_L}{\mathrm{K}_{sb}} + \frac{3w_L}{\overline{R_p}}} \tag{2}$$

where K_{sg} and K_{sb} are the surface/gas phase and surface/bulk aqueous phase equilibrium constants, respectively. The ratio $\frac{\mathrm{K}_{sg}}{\mathrm{K}_{sb}}$ can be viewed as the effective Henry's law constant. w_L is the liquid water mixing ratio in the air and $\overline{R_p}$ is the volume-weighted average radius of the droplets. For PA in the present study, Fig. S1 indicates that the smaller the droplet, the higher the fraction of PA that resides on the surface.

If the sole source of OH is from the gas phase (thus ignoring possible aqueous-phase photolysis reactions[20,22]), multiphase OH oxidation can be divided into sequential processes: gas-phase reaction, gas-surface adsorption/desorption, surface reaction, surface-bulk aqueous transport, and bulk aqueous phase reaction. Given reaction rate constants in the gas phase, on the surface, and in the aqueous phase, the following questions concerning oxidation of a surface-active species arise: What is the rate-limiting step in ambient OH multiphase oxidation? Is the gas-surface-bulk system always at equilibrium? What is the major sink of surface-active species?

The FIDI studies simulate processes occurring within 1 min with an equivalent OH exposure of 1 day under typical ambient conditions. Within a relatively short period, interfacial transport is the rate-limiting step under extremely high OH levels (Fig. 6d). For ambient

OH levels, the conclusion that OH oxidation of PA occurs predominately at the air-water interface may not be directly extrapolated to typical environmental conditions. To clarify this point, we apply the derived rate constant of PA + OH in a case study simulation of the ambient OH oxidation of PA in cloud and fog droplets.

We assume an air parcel with a typical liquid water mixing ratio $w_L = 3 \times 10^{-7}$, [49] equivalent to $\sim$0.6 cm^{-3} droplets of 100 μm diameter or $\sim 5 \times 10^3$ cm^{-3} droplets of 5 μm diameter (Fig. S10a), and an overall PA concentration of 0.5 nmol m^{-3} ($\sim$100 ng m^{-3}).[62,63] The gas-phase OH concentration is assumed constant, 1×10^6 molec cm^{-3}. The multiphase reactions are studied in two ambient cloud droplet sizes,[49,64] i.e., 5 μm and 100 μm. The reaction of PA + OH occurs in the gas phase,[17] on the surface, and in the bulk aqueous phase[20] with rate constants of 1.125×10^{-11} molec^{-1} cm^3 s^{-1}, 9.38×10^{-8} molec^{-1} cm^2 s^{-1}, and 3.30×10^9 M^{-1} s^{-1}, respectively. The fractions of remaining PA in the gas phase, on the surface, and in the bulk aqueous phase are tracked. Initial partitioning of PA between the surface/air and surface/water is at equilibrium (see SI.VIII for detailed calculation), indicating that >99% of PA remains on the surface of a 5 μm droplet, while $\sim$90% remains on the surface of a 100 μm droplet.

By matching the mass flux through the interface with accommodation coefficients and relating the gas phase to the aqueous phase via Henry's law constants,[49,65] one can, in a simplified model, exclude the effect of the interfacial reaction. To distinguish between the two models, we call the former M1 and the latter M2. To minimize the effect of interfacial transport in M2, we adopt the accommodation coefficients as unity for PA, PA products, and OH. The effective Henry's law constant is $H = \frac{\mathrm{K}_{sg}}{\mathrm{K}_{sb}} = 1.95 \times 10^7$ M atm^{-1} for PA and PA products, consistent with that reported in Lignell et al.[22], and 39 M atm^{-1} for OH.[37] As opposed to M1, partition of PA between gas phase and aqueous phase at equilibrium[59] in M2 is independent of droplet size ($F_{\mathrm{aq}} = \frac{Hw_L}{1+Hw_L} > 99\%$), and diffusion of OH inside the droplet is found to be the rate-limiting step of the multiphase oxidation.

For both models, an overall simulation time is taken as 12 h, corresponding to an equiv-

alent OH exposure as used in the FIDI experiments. Shrinkage or growth of the droplets is not considered during the 12 h simulation, given that water vapor is at equilibrium in the cloud.

Figures 7a and b present the predicted fractions of different PA fates in the systems in droplets of 5 μm and 100 μm, respectively. Since the surface properties of PA and PA products are identical in M1, the constant fraction of the sum of PA and PA products within any phase during the simulation indicates that the partitioning of PA and PA products between the gas phase, the surface, and the bulk aqueous phase remains at equilibrium. This quasi-equilibrium partitioning can be attributed to the fact that the reaction rates are sufficiently slow (because of the relatively low OH concentration) such that mass transport between the gas phase, the surface, and the bulk aqueous phase is no longer a rate-limiting step. The consumption of PA in the 5 μm system occurs exclusively at the air-water interface, while $\sim$10% is contributed by the aqueous-phase OH oxidation in the 100 μm system. Both Fig. 7a and b suggest that gas-phase oxidation of PA is unimportant in the cloud and fog system, which also applies to M2, i.e., without accounting for interfacial effects, aqueous phase oxidation predominates.

The simulated bulk aqueous-phase OH distributions (Fig. 7c) suggest that the smaller the droplet, the more uniform the bulk. For larger droplets, the reaction is constrained to the sub-surface region, which is characterized by the OH reactive-diffusive length (EQ. (1)), since less PA resides on the surface leaving the bulk aqueous-phase with relatively stronger OH reactivity ($k_b^{OH+PA}C_b^{PA}$). The OH uptake coefficient by 5 μm droplet surface is $\sim$1 order of magnitude smaller than that by 100 μm droplet surface (Fig. S10b). However, given the much larger surface area concentration in the 5 μm droplet system, under the same OH exposure, the overall PA concentration is predicted to decay $\sim$90%, higher than $\sim$75% in the 100 μm droplet system (Fig. 7d). By comparison, if the interfacial interaction is not considered (M2), the model predictions suggest that PA is depleted in $\sim$30 min in the 5 μm system and $\sim$6 h in the 100 μm system. The longer lifetime of PA in the larger droplet system

reflects the fact that in the absence of the interfacial resistance, i.e., interfacial reaction and accommodation, the rate-limiting step is bulk aqueous-phase diffusion of OH.

Conclusions

Interfacial effects of surfactants have been recognized to lower the surface tension and facilitate cloud droplet formation.[66,67] The present case study highlights the significance of air-water interfacial partitioning and reaction of surface-active species, e.g., PA. For the cloud and fog system with characteristically higher air-water surface area concentration, the sink of the surface-active species can be expected to occur predominantly on the surface, so that the surface reaction rate is the rate-limiting step in the multiphase OH oxidation. The quasi-equilibrium partitioning state during the oxidation suggests that in the absence of a source of surface-active species (either from outside of the air parcel or from oxidation of precursors), multiphase OH oxidation can be simplified as occurring in three individual regions (gas phase, surface, and bulk aqueous phase), for which, the explicit dynamic multiphase model developed here applies. For species that are less surface-active, e.g., glyoxal,[59,68,69] the effect of air-water interfacial processes may not be as significant as those for surface-active species. Since the simulation treats the gas-phase OH as the sole source, given the high solubility of H_2O_2 (Henry's law constant = 8.70×10^4 at 298 K),[70] potential photolysis of dissolved H_2O_2 can serve as a large source of aqueous-phase OH[71] and the fate of surface-active species may change. Moreover, photosensitized chemistry has been proved to play a critical role on the radical-radical reaction at the air-water interface.[72–74] Additional studies are needed to clarify the competitive OH oxidations of surface-active species among gas phase, surface, and bulk aqueous phase under different conditions.

Table 1: Parameters and Reaction Rate Constants Used in This Work

Symbol	Parameter	Value
α_s^i	surface accommodation coefficient for species i	1
δ	interface thickness (m)	6.9×10^{-10} [37]
$\mathcal{D}_g^{OH}$	gas-phase OH diffusivity ($m^2\ s^{-1}$)	2.67×10^{-5}
$\mathcal{D}_b^{OH}$	aqueous-phase OH diffusivity ($m^2\ s^{-1}$)	2.30×10^{-9} [75]
$\mathcal{D}_b^{PA}$	aqueous-phase PA diffusivity ($m^2\ s^{-1}$)	1×10^{-10}
K_{sg}^{OH}	surface-gas adsorption equilibrium constant of OH (m)	6.07×10^{-6} [37]
K_{sb}^{OH}	surface-bulk adsorption equilibrium constant of OH (m)	5.52×10^{-9} [37]
K_{sg}^{PA}	surface-gas adsorption equilibrium constant of PA (m)	9.62×10^{4}
K_{sb}^{PA}	surface-bulk adsorption equilibrium constant of PA (m)	2.01×10^{-4}
$k_{\text{bulk}}^{\text{OH+PA}}$	bulk reaction rate constant of OH + PA ($M^{-1}\ s^{-1}$)	3.30×10^{9} [20]
$k_{\text{surf}}^{\text{OH+SDS}}$	surface reaction rate constant of OH + SDS ($cm^2\ molec^{-1}\ s^{-1}$)	2.87×10^{-8} [a]
$k_{\text{surf}}^{\text{OH+PA}}$	surface reaction rate constant of OH + PA ($cm^2\ molec^{-1}\ s^{-1}$)	9.38×10^{-8} [a]

[a] These values are from fitting of the experimental data. Refer to Results and Discussion for details.

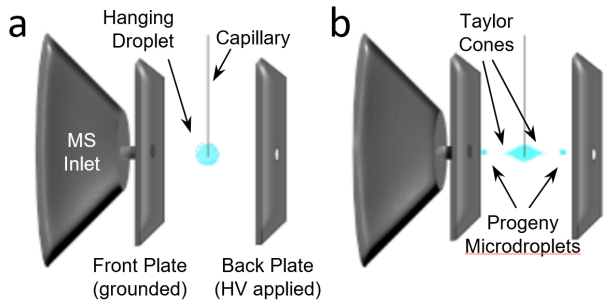

Figure 1: Schematic of FIDI-MS for oxidation studies, as viewed from the side. a: A droplet hanging between two parallel plate electrodes. b: A snapshot of the elongated droplet when the pulsed voltage is employed to the plate electrodes.

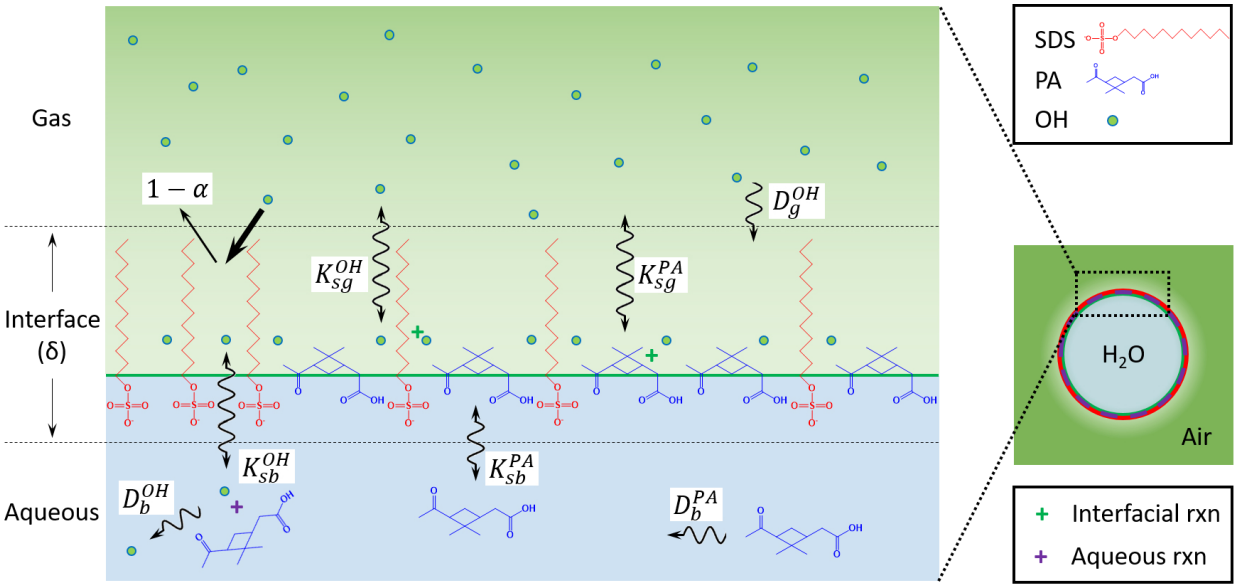

Figure 2: Multiphase transport and reaction model for OH reaction with sodium dodecyl sulfate (SDS) and pinonic acid (PA) at the air-water interface. Key parameters of corresponding processes are labeled and explanation can be found in SI.I and Table 1.

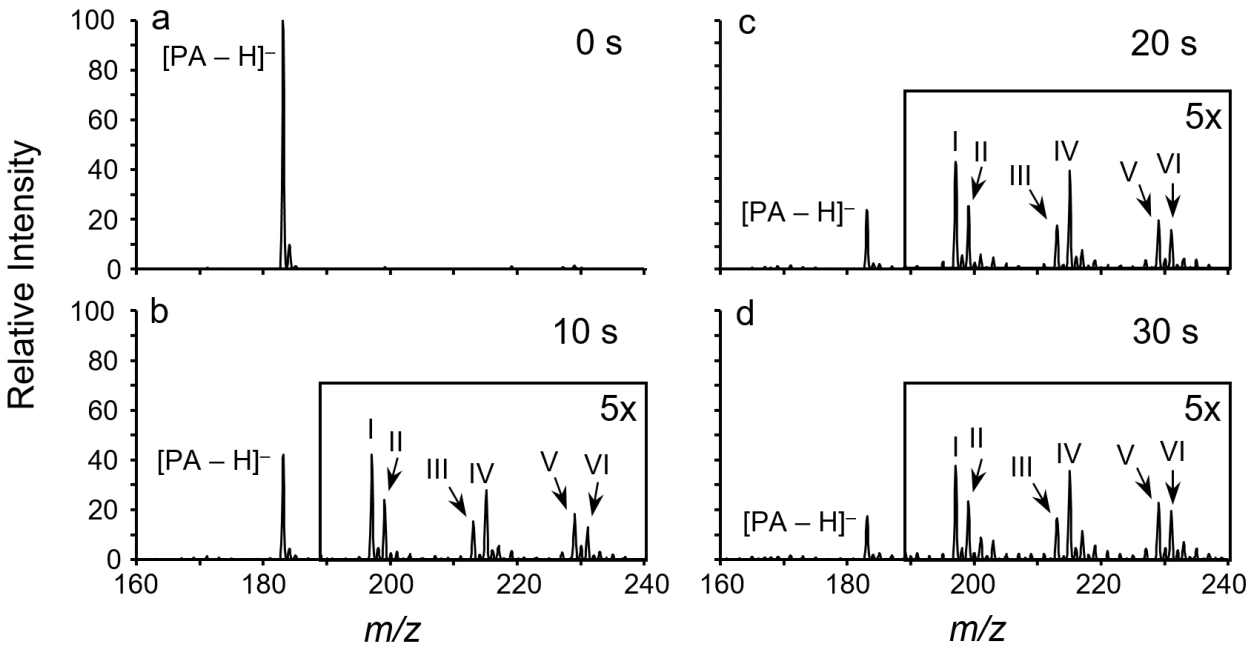

Figure 3: Pinonic acid (PA) oxidation at the air-water interface by gas-phase OH detected by FIDI-MS OH exposure. a. 0 s; b. 10 s; c. 20 s; d. 30 s. m/z of identified products are as follows: I = 197, II = 199, III = 213, IV = 215, V = 229, and VI = 231. Mass spectra are reported as averages of replicate samples (N = 5). The peak intensities in b, c, and d have been normalized with respect to the peak intensity of $[PA-H]^-$ in a.

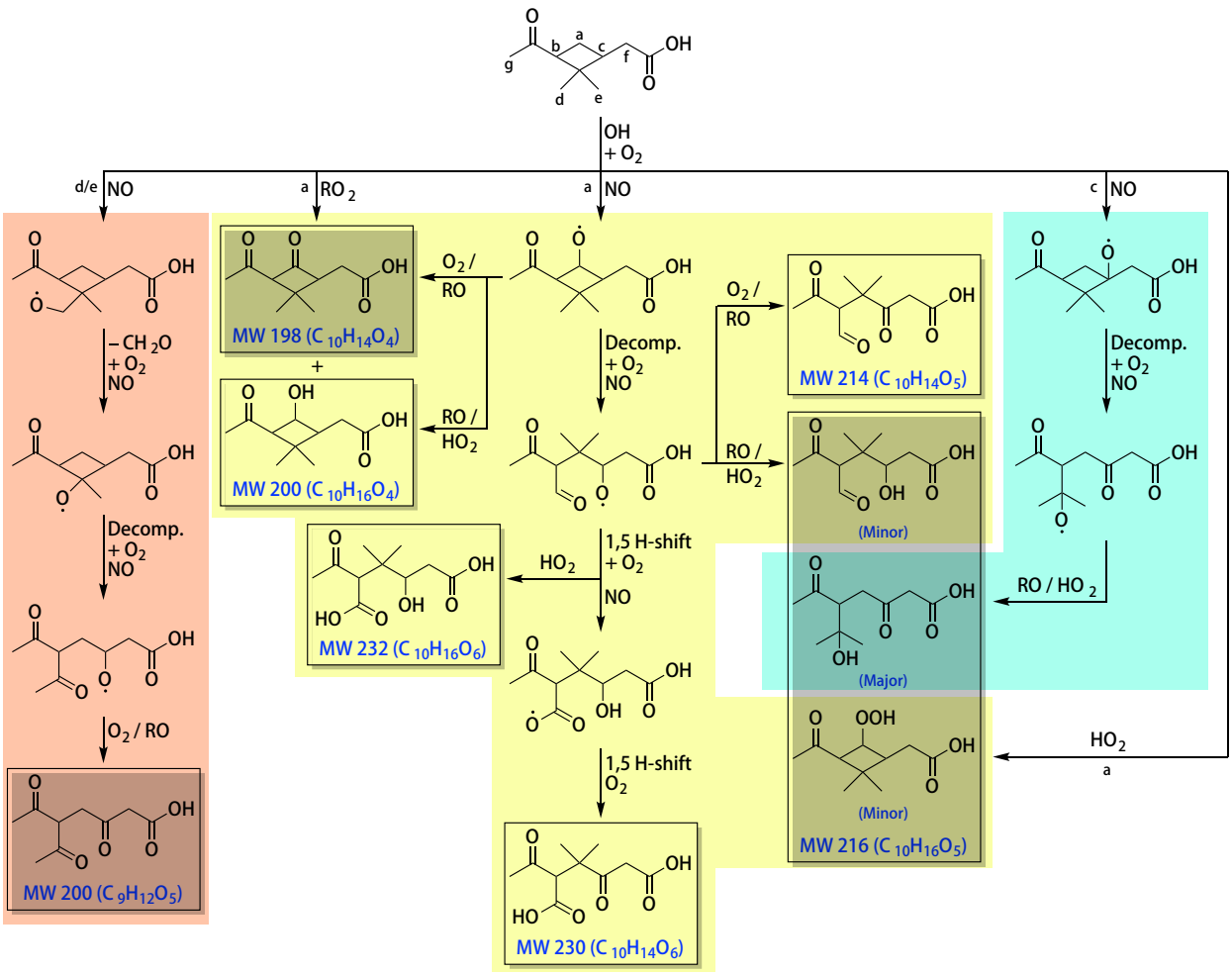

Figure 4: Mechanism of OH-initiated oxidation of PA under NO-dominant conditions.

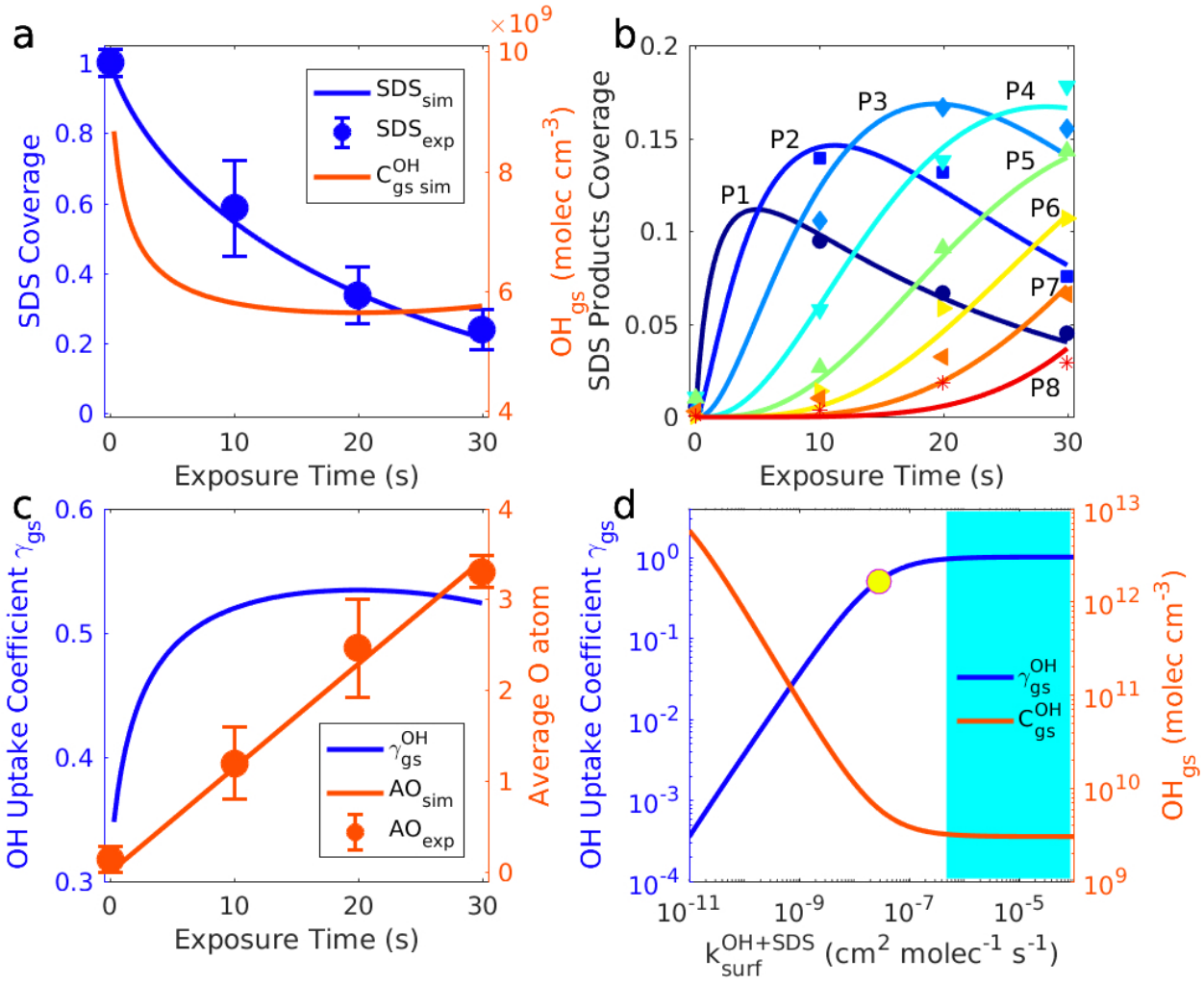

Figure 5: Experimental and fitted results of the OH oxidation of the SDS droplet. a. Temporal profiles of SDS coverage (blue dots, measured values averaged by 5 repeats; blue line, fitting result) and the modeling gas-phase OH concentration above the surface (orange line). b. Temporal profiles of 8 generations of SDS + OH products (lines are fitting results and dots are experimental results). c. Temporal profiles of predicted OH uptake coefficient (blue line) and the average number of oxygen atoms incorporated into SDS via OH oxidation (orange dots, measured values averaged by 5 repeats; orange line, fitting result). d. Calculated OH uptake coefficient and the gas-phase OH concentration above the surface as a function of the optimally fitted surface reaction rate constant for SDS + OH system. Yellow dot represents the value adopted in this study and cyan background marks the gas-phase diffusion limit regime for the determination of $k_{\mathrm{surf}}^{\mathrm{OH+SDS}}$.

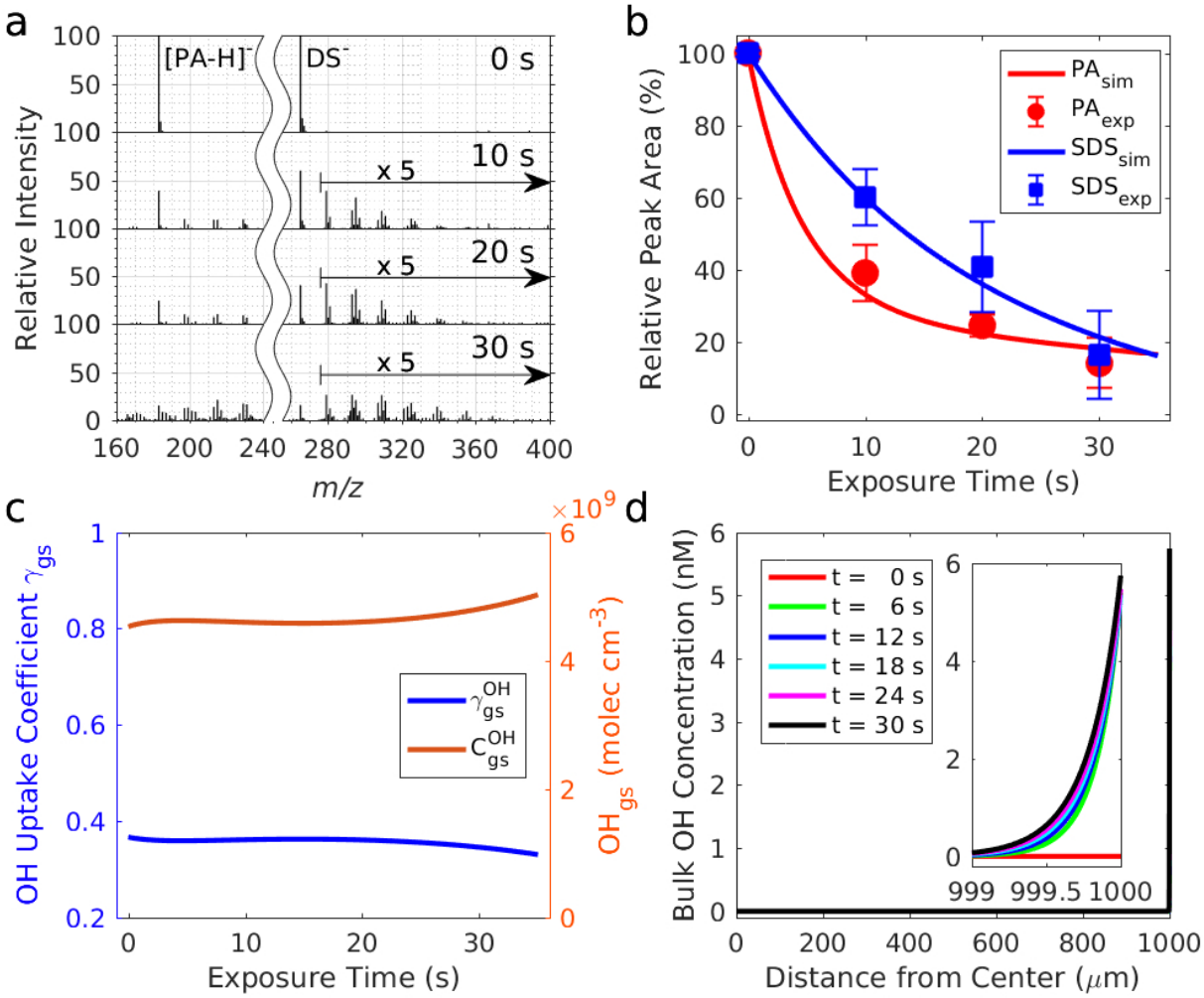

Figure 6: Experimental and simulation results of the OH oxidation of the mixture of PA and SDS droplet. a. Mass spectra of the sampling under different OH exposure (left is the PA regime and right is the SDS regime). b. Temporal profiles of the surface coverage of PA and SDS. Dots represent experimental measurements (averaged by 5 repeats) and lines represent simulated results. c. Predicted temporal profiles of the OH uptake coefficient and the gas-phase OH concentration. d. Simulated bulk aqueous-phase OH distribution at different exposure time. Inset panel is the zoom-in near the surface regime.

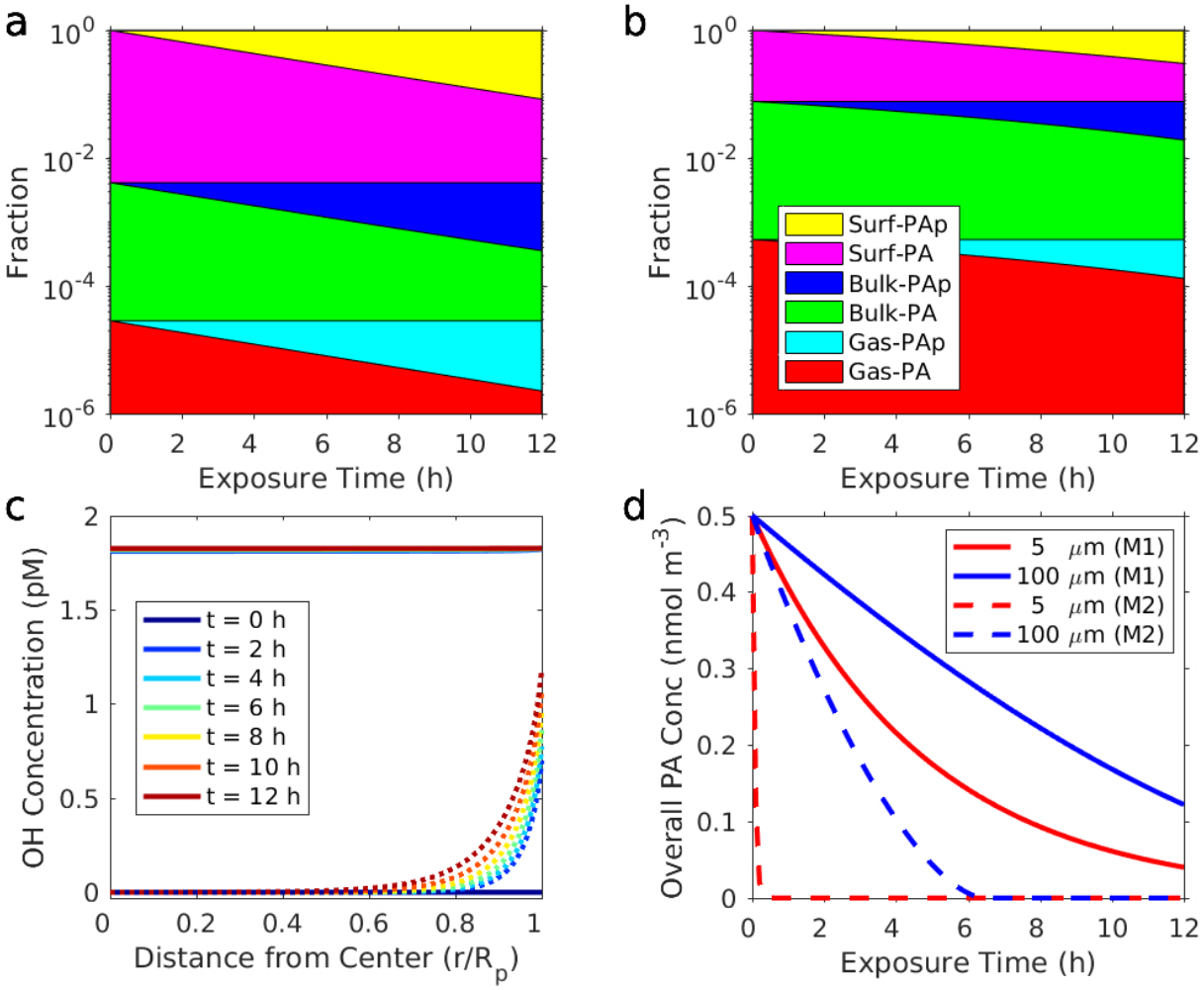

Figure 7: Simulated multi-phase OH oxidation of PA in droplets of 5 μm (a) and 100 μm (b), with an overall PA concentration of 0.5 nmol m^{-3} under typical ambient conditions (gas-phase OH concentration $\sim 10^6$ molec cm^{-3}). a and b: Fraction of the overall quantities of PA and PA products that resides on the surface, in the bulk aqueous phase, and in the gas phase. c: Predicted bulk aqueous-phase distribution of OH at different OH exposure times by M1 (solid lines: 5 μm droplets, dashed lines: 100 μm droplets). d: Temporal profiles of overall PA as exposed to OH.

Acknowledgement

This work was supported, in part, by National Science Foundation grant AGS-1523500. RZ acknowledges support from Natural Science and Engineering Research Council of Canada Postdoctoral Fellowship (NSERC-PDF). CW acknowledges helpful discussion on COSMOtherm surface partitioning predictions with Dr. Jens Reinisch and Dr. Frank Eckert from COSMOlogic.

Supporting Information Available

The supplementary material contains eight sections, i.e., I. Model Description, II. Surface Coverage of PA at Surface-Bulk Equilibrium, III. Air-Surface-Water Equilibrium Constants, IV. Evaporation of PA from Droplet, V. Identification of PA + OH Products, VI. SDS + OH Fitting, VII. PA + OH and SDS + OH Fitting, and VIII. Droplet Simulation.

This material is available free of charge via the Internet at `http://pubs.acs.org/`.

References

(1) George, I. J.; Abbatt, J. P. D. Heterogeneous Oxidation of Atmospheric Aerosol Particles by Gas-Phase Radicals. *Nat. Chem.* **2010**, *2*, 713.

(2) Houle, F. A.; Wiegel, A. A.; Wilson, K. R. Changes in Reactivity as Chemistry Becomes Confined to an Interface. The Case of Free Radical Oxidation of $C_{30}H_{62}$ Alkane by OH. *J. Phys. Chem. Lett* **2018**, *9*, 1053–1057.

(3) Zhong, J.; Kumar, M.; Francisco, J. S.; Zeng, X. C. Insight into Chemistry on Cloud/Aerosol Water Surfaces. *Acc. Chem. Res.* **2018**, *51*, 1229–1237.

(4) Wren, S. N.; Gordon, B. P.; Valley, N. A.; McWilliams, L. E.; Richmond, G. L. Hy-

dration, Orientation, and Conformation of Methylglyoxal at the Air-Water Interface. *J. Phys. Chem. A* **2015**, *119*, 6391–6403.

(5) Heath, A. A.; Valsaraj, K. T. Effects of Temperature, Oxygen Level, Ionic Strength, and pH on the Reaction of Benzene with Hydroxyl Radicals at the Air-Water Interface in Comparison to the Bulk Aqueous Phase. *J. Phys. Chem. A* **2015**, *119*, 8527–8536.

(6) Hua, W.; Verreault, D.; Allen, H. C. Relative Order of Sulfuric Acid, Bisulfate, Hydronium, and Cations at the Air-Water Interface. *J. Am. Chem. Soc.* **2015**, *137*, 13920–13926.

(7) Martins-Costa, M. T. C.; García-Prieto, F. F.; Ruiz-López, M. F. Reactivity of Aldehydes at the Air-Water Interface. Insights from Molecular Dynamics Simulations and ab initio Calculations. *Org. Biomol. Chem.* **2015**, *13*, 1673–1679.

(8) Enami, S.; Colussi, A. J. Efficient Scavenging of Criegee Intermediates on Water by Surface-Active *cis*-pinonic Acid. *Phys. Chem. Chem. Phys.* **2017**, *19*, 17044–17051.

(9) Jones, S. H.; King, M. D.; Ward, A. D.; Rennie, A. R.; Jones, A. C.; Arnold, T. Are Organic Films from Atmospheric Aerosol and Sea Water Inert to Oxidation by Ozone at the Air-Water Interface? *Atmos. Environ.* **2017**, *161*, 274–287.

(10) Wellen, B. A.; Lach, E. A.; Allen, H. C. Surface pK_a of Octanoic, Nonanoic, and Decanoic Fatty Acids at the Air-Water Interface: Applications to Atmospheric Aerosol Chemistry. *Phys. Chem. Chem. Phys.* **2017**, *19*, 26551–26558.

(11) Kumar, M.; Li, H.; Zhang, X.; Zeng, X. C.; Francisco, J. S. Nitric Acid-Amine Chemistry in the Gas Phase and at the Air-Water Interface. *J. Am. Chem. Soc.* **2018**,

(12) Pillar, E. A.; Guzman, M. I. Oxidation of Substituted Catechols at the Air-Water Interface: Production of Carboxylic Acids, Quinones, and Polyphenols. *Environ. Sci. Technol.* **2017**, *51*, 4951–4959.

(13) King, M. D.; Rennie, A. R.; Thompson, K. C.; Fisher, F. N.; Dong, C. C.; Thomas, R. K.; Pfrang, C.; Hughes, A. V. Oxidation of Oleic Acid at the Air-Water Interface and Its Potential Effects on Cloud Critical Supersaturations. *Phys. Chem. Chem. Phys.* **2009**, *11*, 7699–7707.

(14) Xiao, P.; Wang, Q.; Fang, W.-H.; Cui, G. Quantum Chemical Investigation on Photochemical Reactions of Nonanoic Acids at Air-Water Interface. *J. Phys. Chem. A* **2017**, *121*, 4253–4262.

(15) Sebastiani, F.; Campbell, R. A.; Rastogi, K.; Pfrang, C. Nighttime Oxidation of Surfactants at the Air-Water Interface: Effects of Chain Length, Head Group and Saturation. *Atmos. Chem. Phys.* **2018**, *18*, 3249–3268.

(16) Guenther, A. B.; Jiang, X.; Heald, C. L.; Sakulyanontvittaya, T.; Duhl, T.; Emmons, L. K.; Wang, X. The Model of Emissions of Gases and Aerosols from Nature version 2.1 (MEGAN2.1): An Extended and Updated Framework for Modeling Biogenic Emissions. *Geosci. Model Dev.* **2012**, *5*, 1471–1492.

(17) Müller, L.; Reinnig, M.-C.; Naumann, K. H.; Saathoff, H.; Mentel, T. F.; Donahue, N. M.; Hoffmann, T. Formation of 3-Methyl-1,2,3-Butanetricarboxylic Acid via Gas Phase Oxidation of Pinonic Acid - A Mass Spectrometric Study of SOA Aging. *Atmos. Chem. Phys.* **2012**, *12*, 1483–1496.

(18) Witkowski, B.; Gierczak, T. *cis*-Pinonic Acid Oxidation by Hydroxyl Radicals in the Aqueous Phase under Acidic and Basic Conditions: Kinetics and Mechanism. *Environ. Sci. Technol.* **2017**, *51*, 9765–9773.

(19) Lee, A. K. Y.; Herckes, P.; Leaitch, W. R.; Macdonald, A. M.; Abbatt, J. P. D. Aqueous OH Oxidation of Ambient Organic Aerosol and Cloud Water Organics: Formation of Highly Oxidized Products. *Geophys. Res. Lett.* **2011**, *38*, L11805.

(20) Aljawhary, D.; Zhao, R.; Lee, A. K. Y.; Wang, C.; Abbatt, J. P. D. Kinetics, Mechanism, and Secondary Organic Aerosol Yield of Aqueous Phase Photo-Oxidation of α-Pinene Oxidation Products. *J. Phys. Chem. A* **2016**, *120*, 1395–1407.

(21) Bilde, M.; Pandis, S. N. Evaporation Rates and Vapor Pressures of Individual Aerosol Species Formed in the Atmospheric Oxidation of α- and β-Pinene. *Environ. Sci. Technol.* **2001**, *35*, 3344–3349.

(22) Lignell, H.; Epstein, S. A.; Marvin, M. R.; Shemesh, D.; Gerber, B.; Nizkorodov, S. Experimental and Theoretical Study of Aqueous *cis*-Pinonic Acid Photolysis. *J. Phys. Chem. A* **2013**, *117*, 12930–12945.

(23) Li, X.; Hede, T.; Tu, Y.; Leck, C.; Ågren, H. Surface-Active *cis*-Pinonic Acid in Atmospheric Droplets: A Molecular Dynamics Study. *J. Phys. Chem. Lett.* **2010**, *1*, 769–773.

(24) Enami, S.; Sakamoto, Y. OH-Radical Oxidation of Surface-Active *cis*-Pinonic Acid at the Air-Water Interface. *J. Phys. Chem. A* **2016**, *120*, 3578–3587.

(25) Lai, C.; Liu, Y.; Ma, J.; Ma, Q.; Chu, B.; He, H. Heterogeneous Kinetics of *cis*-Pinonic Acid with Hydroxyl Radical under Different Environmental Conditions. *J. Phys. Chem. A* **2015**, *119*, 6583–6593.

(26) Grimm, R. L.; Beauchamp, J. L. Field-Induced Droplet Ionization Mass Spectrometry. *J. Phys. Chem. B* **2003**, *107*, 14161–14163.

(27) Grimm, R. L.; Beauchamp, J. L. Dynamics of Field-Induced Droplet Ionization: Time-Resolved Studies of Distortion, Jetting, and Progeny Formation from Charged and Neutral Methanol Droplets Exposed to Strong Electric Fields. *J. Phys. Chem. B* **2005**, *109*, 8244–8250.

(28) Grimm, R. L.; Hodyss, R.; Beauchamp, J. L. Probing Interfacial Chemistry of Single Droplets with Field-Induced Droplet Ionization Mass Spectrometry: Physical Adsorp-

tion of Polycyclic Aromatic Hydrocarbons and Ozonolysis of Oleic Acid and Related Compounds. *Anal. Chem.* **2006**, *78*, 3800–3806.

(29) Thomas, D. A.; Coggon, M. M.; Lignell, H.; Schilling, K. A.; Zhang, X.; Schwantes, R. H.; Flagan, R. C.; Seinfeld, J. H.; Beauchamp, J. L. Real-Time Studies of Iron Oxalate-Mediated Oxidation of Glycolaldehyde as a Model for Photochemical Aging of Aqueous Tropospheric Aerosols. *Environ. Sci. Technol.* **2016**, *50*, 12241–12249.

(30) Zhang, X.; Barraza, K. M.; Upton, K. T.; Beauchamp, J. L. Time Resolved Study of Hydroxyl Radical Oxidation of Oleic Acid at the Air-Water Interface. *Chem. Phys. Lett.* **2017**, *683*, 76–82.

(31) Kim, H. I.; Kim, H.; Shin, Y. S.; Beegle, L. W.; Goddard, W. A.; Heath, J. R.; Kanik, I.; Beauchamp, J. L. Time Resolved Studies of Interfacial Reactions of Ozone with Pulmonary Phospholipid Surfactants Using Field Induced Droplet Ionization Mass Spectrometry. *J. Phys. Chem. B* **2010**, *114*, 9496–9503.

(32) Kim, H. I.; Kim, H.; Shin, Y. S.; Beegle, L. W.; Jang, S. S.; Neidholdt, E. L.; Goddard, W. A.; Heath, J. R.; Kanik, I.; Beauchamp, J. L. Interfacial Reactions of Ozone with Surfactant Protein B in a Model Lung Surfactant System. *J. Am. Chem. Soc.* **2010**, *132*, 2254–2263.

(33) Zhang, X.; Barraza, K. M.; Beauchamp, J. L. Cholesterol Provides Nonsacrificial Protection of Membrane Lipids from Chemical Damage at Air-Water Interface. *Proc. Natl. Acad. Sci. U. S. A.* **2018**, 201722323.

(34) Barraza, K. M. The Study of the Stepwise Hydroxyl Radical-Mediated Oxidation of Alkyl Surfactants at the Air-Water Interface. Ph.D. thesis, California Institute of Technology, 2018.

(35) Pöschl, U.; Rudich, Y.; Ammann, M. Kinetic Model Framework for Aerosol and Cloud

Surface Chemistry and Gas-Particle Interactions - Part 1: General Equations, Parameters, and Terminology. *Atmos. Chem. Phys.* **2007**, *7*, 5989–6023.

(36) Socorro, J.; Lakey, P. S. J.; Han, L.; Berkemeier, T.; Lammel, G.; Zetzsch, C.; Pöschl, U.; Shiraiwa, M. Heterogeneous OH Oxidation, Shielding Effects, and Implications for the Atmospheric Fate of Terbuthylazine and Other Pesticides. *Environ. Sci. Technol.* **2017**, *51*, 13749–13754.

(37) Vácha, R.; Slavíček, P.; Mucha, M.; Finlayson-Pitts, B. J.; Jungwirth, P. Adsorption of Atmospherically Relevant Gases at the Air/Water Interface: Free Energy Profiles of Aqueous Solvation of N_2, O_2, O_3, OH, H_2O, HO_2, and H_2O_2. *J. Phys. Chem. A* **2004**, *108*, 11573–11579.

(38) Svishchev, I. M.; Plugatyr, A. Y. Hydroxyl Radical in Aqueous Solution: Computer Simulation. *J. Phys. Chem. B* **2005**, *109*, 4123–4128.

(39) Goss, K.-U. Predicting Adsorption of Organic Chemicals at the Air-Water Interface. *J. Phys. Chem. A* **2009**, *113*, 12256–12259.

(40) Wang, C.; Goss, K.-U.; Lei, Y. D.; Abbatt, J. P. D.; Wania, F. Calculating Equilibrium Phase Distribution during the Formation of Secondary Organic Aerosol Using COSMOtherm. *Environ. Sci. Technol.* **2015**, *49*, 8585–8594.

(41) Vereecken, L.; Peeters, J. Enhanced H-Atom Abstraction from Pinonaldehyde, Pinonic Acid, Pinic Acid, and Related Compounds: Theoretical Study of C-H Bond Strengths. *Phys. Chem. Chem. Phys.* **2002**, *4*, 467–472.

(42) Atkinson, R.; Arey, J. Atmospheric Degradation of Volatile Organic Compounds. *Chem. Rev.* **2003**, *103*, 4605–4638.

(43) Orlando, J. J.; Tyndall, G. S. Laboratory Studies of Organic Peroxy Radical Chemistry:

An Overview with Emphasis on Recent Issues of Atmospheric Significance. *Chem. Soc. Rev.* **2012**, *41*, 6294–6317.

(44) von Sonntag, C.; Schuchmann, H.-P. The Elucidation of Peroxyl Radical Reactions in Aqueous Solution with the Help of Radiation-Chemical Methods. *Angew. Chem. Int. Ed.* **1991**, *30*, 1229–1253.

(45) Ervens, B.; Volkamer, R. Glyoxal Processing by Aerosol Multiphase Chemistry: Towards a Kinetic Modeling Framework of Secondary Organic Aerosol Formation in Aqueous Particles. *Atmos. Chem. Phys.* **2010**, *10*, 8219–8244.

(46) California Air Resources Board. Air Quality and Meteorological Information System. `https://www.arb.ca.gov/aqmis2/aqdselect.php`.

(47) Praske, E.; Otkjær, R. V.; Crounse, J. D.; Hethcox, J. C.; Stoltz, B. M.; Kjaergaard, H. G.; Wennberg, P. O. Atmospheric Autoxidation is Increasingly Important in Urban and Suburban North America. *Proc. Natl. Acad. Sci. U. S. A.* **2017**, 201715540.

(48) Carslaw, N. A New Detailed Chemical Model for Indoor Air Pollution. *Atmos. Environ.* **2007**, *41*, 1164–1179.

(49) Seinfeld, J. H.; Pandis, S. N. *Atmospheric Chemistry and Physics: From Air Pollution to Climate Change*, 3rd ed.; Wiley Sons, 2016.

(50) Yasmeen, F.; Vermeylen, R.; Szmigielski, R.; Iinuma, Y.; Böge, O.; Herrmann, H.; Maenhaut, W.; Claeys, M. Terpenylic Acid and Related Compounds: Precursors for Dimers in Secondary Organic Aerosol from the Ozonolysis of α- and β-Pinene. *Atmos. Chem. Phys.* **2010**, *10*, 9383–9392.

(51) Demarque, D. P.; Crotti, A. E. M.; Vessecchi, R.; Lopes, J. L. C.; Lopes, N. P. Fragmentation Reactions Using Electrospray Ionization Mass Spectrometry: An Important Tool

for the Structural Elucidation and Characterization of Synthetic and Natural Products. *Nat. Prod. Rep.* **2016**, *33*, 432–455.

(52) Russell, G. A. Deuterium-Isotope Effects in the Autoxidation of Aralkyl Hydrocarbons. Mechanism of the Interaction of Peroxy Radicals. *J. Am. Chem. Soc.* **1957**, *79*, 3871–3877.

(53) Howell, H.; Fisher, G. S. The Dissociation Constants of Some of the Terpene Acids. *J. Am. Chem. Soc* **1958**, *80*, 6316–6319.

(54) Ervens, B.; Gligorovski, S.; Herrmann, H. Temperature-Dependent Rate Constants for Hydroxyl Radical reactions with Organic Compounds in Aqueous Solutions. *Phys. Chem. Chem. Phys.* **2003**, *5*, 1811–1824.

(55) Lee, M.-T.; Orlando, F.; Artiglia, L.; Chen, S.; Ammann, M. Chemical Composition and Properties of the Liquid-Vapor Interface of Aqueous C1 to C4 Monofunctional Acid and Alcohol Solutions. *J. Phys. Chem. A* **2016**, *120*, 9749–9758.

(56) Tan, A.; Ziegler, A.; Steinbauer, B.; Seelig, J. Thermodynamics of Sodium Dodecyl Sulfate Partitioning into Lipid Membranes. *Biophys. J.* **2002**, *83*, 1547–1556.

(57) Blando, J. D.; Turpin, B. J. Secondary Organic Aerosol Formation in Cloud and Fog Droplets: a Literature Evaluation of Plausibility. *Atmos. Environ.* **2000**, *34*, 1623–1632.

(58) Lim, Y. B.; Tan, Y.; Perri, M. J.; Seitzinger, S. P.; Turpin, B. J. Aqueous Chemistry and Its Role in Secondary Organic Aerosol (SOA) Formation. *Atmos. Chem. Phys.* **2010**, *10*, 10521–10539.

(59) Ervens, B.; Turpin, B. J.; Weber, R. J. Secondary Organic Aerosol Formation in Cloud Droplets and Aqueous Particles (aqSOA): A Review of Laboratory, Field and Model Studies. *Atmos. Chem. Phys.* **2011**, *11*, 11069–11102.

(60) Lim, H.-J.; Carlton, A. G.; Turpin, B. J. Isoprene Forms Secondary Organic Aerosol through Cloud Processing: Model Simulations. *Environ. Sci. Technol.* **2005**, *39*, 4441–4446.

(61) McNeill, V. F.; Woo, J. L.; Kim, D. D.; Schwier, A. N.; Wannell, N. J.; Sumner, A. J.; Barakat, J. M. Aqueous-Phase Secondary Organic Aerosol and Organosulfate Formation in Atmospheric Aerosols: A Modeling Study. *Environ. Sci. Technol.* **2012**, *46*, 8075–8081.

(62) Kavouras, I. G.; Mihalopoulos, N.; Stephanou, E. G. Secondary Organic Aerosol Formation vs Primary Organic Aerosol Emission: In Situ Evidence for the Chemical Coupling between Monoterpene Acidic Photooxidation Products and New Particle Formation over Forests. *Environ. Sci. Technol.* **1999**, *33*, 1028–1037.

(63) Vestenius, M.; Hellén, H.; Levula, J.; Kuronen, P.; Helminen, K. J.; Nieminen, T.; Kulmala, M.; Hakola, H. Acidic Reaction Products of Monoterpenes and Sesquiterpenes in Atmospheric Fine Particles in a Boreal Forest. *Atmos. Chem. Phys.* **2014**, *14*, 7883–7893.

(64) Bréon, F.-M.; Tanré, D.; Generoso, S. Aerosol Effect on Cloud Droplet Size Monitored from Satellite. *Science* **2002**, *295*, 834–838.

(65) Mai, H.; Shiraiwa, M.; Flagan, R. C.; Seinfeld, J. H. Under What Conditions Can Equilibrium Gas-Particle Partitioning Be Expected to Hold in the Atmosphere? *Environ. Sci. Technol.* **2015**, *49*, 11485–11491.

(66) Nozière, B. Don't Forget the Surface. *Science* **2016**, *351*, 1396–1397.

(67) Ruehl, C. R.; Davies, J. F.; Wilson, K. R. An Interfacial Mechanism for Cloud Droplet Formation on Organic Aerosols. *Science* **2016**, *351*, 1447–1450.

(68) Tan, Y.; Perri, M. J.; Seitzinger, S. P.; Turpin, B. J. Effects of Precursor Concentration and Acidic Sulfate in Aqueous Glyoxal-OH Radical Oxidation and Implications for Secondary Organic Aerosol. *Environ. Sci. Technol.* **2009**, *43*, 8105–8112.

(69) Galloway M. M.,; Loza C. L.,; Chhabra P. S.,; Chan A. W. H.,; Yee L. D.,; Seinfeld J. H.,; Keutsch F. N., Analysis of Photochemical and Dark Glyoxal Uptake: Implications for SOA Formation. *Geophys. Res. Lett* **2011**, *38*, L17811.

(70) Burkholder, J. B.; Sander, S. P.; Abbatt, J. P. D.; Barker, J. R.; Huie, R. E.; Kolb, C. E.; Kurylo, M. J.; Orkin, V. L.; Wilmouth, D. M.; Wine, P. H. *Chemical Kinetics and Photochemical Data for Use in Atmospheric Studies, Evaluation No. 18*; JPL Publication 15-10, Jet Propulsion Laboratory, Pasadena, 2015.

(71) Kameel, F. R.; Hoffmann, M. R.; Colussi, A. J. OH Radical-Initiated Chemistry of Isoprene in Aqueous Media. Atmospheric Implications. *J. Phys. Chem. A* **2013**, *117*, 5117–5123.

(72) Tinel, L.; Rossignol, S.; Bianco, A.; Passananti, M.; Perrier, S.; Wang, X.; Brigante, M.; Donaldson, D. J.; George, C. Mechanistic Insights on the Photosensitized Chemistry of a Fatty Acid at the Air/Water Interface. *Environ. Sci. Technol.* **2016**, *50*, 11041–11048.

(73) Bernard, F.; Ciuraru, R.; Boréave, A.; George, C. Photosensitized Formation of Secondary Organic Aerosols above the Air/Water Interface. *Environ. Sci. Technol.* **2016**, *50*, 8678–8686.

(74) Rossignol, S.; Tinel, L.; Bianco, A.; Passananti, M.; Brigante, M.; Donaldson, D. J.; George, C. Atmospheric Photochemistry at a Fatty Acid-Coated Air-Water Interface. *Science* **2016**, *353*, 699–702.

(75) Ivanov, A. V.; Trakhtenberg, S.; Bertram, A. K.; Gershenzon, Y. M.; Molina, M. J. OH, HO_2, and Ozone Gaseous Diffusion Coefficients. *J. Phys. Chem. A* **2007**, *111*, 1632–1637.

Graphical TOC Entry

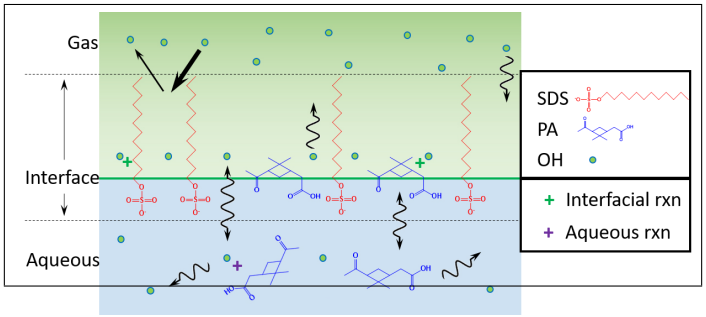

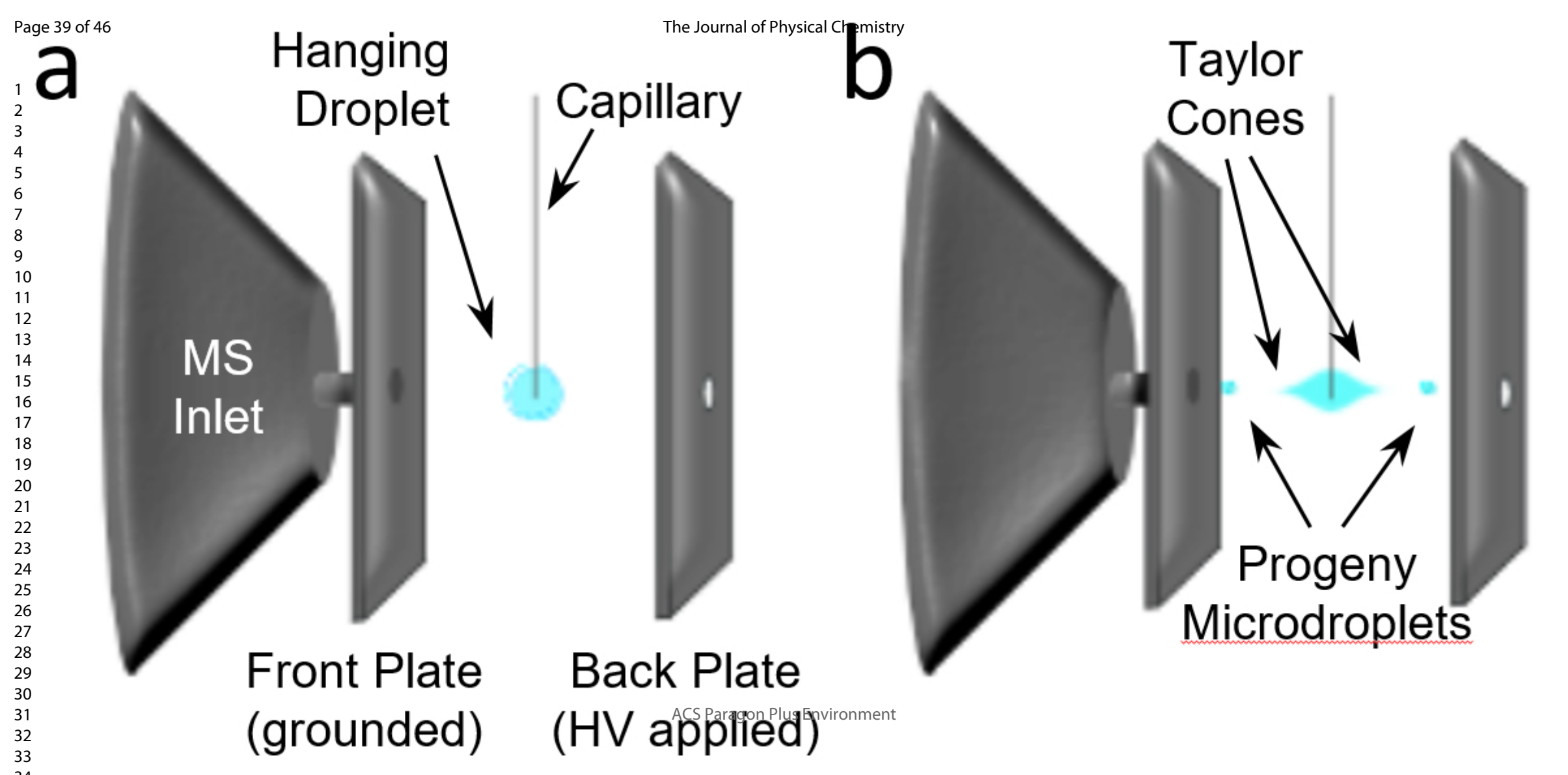

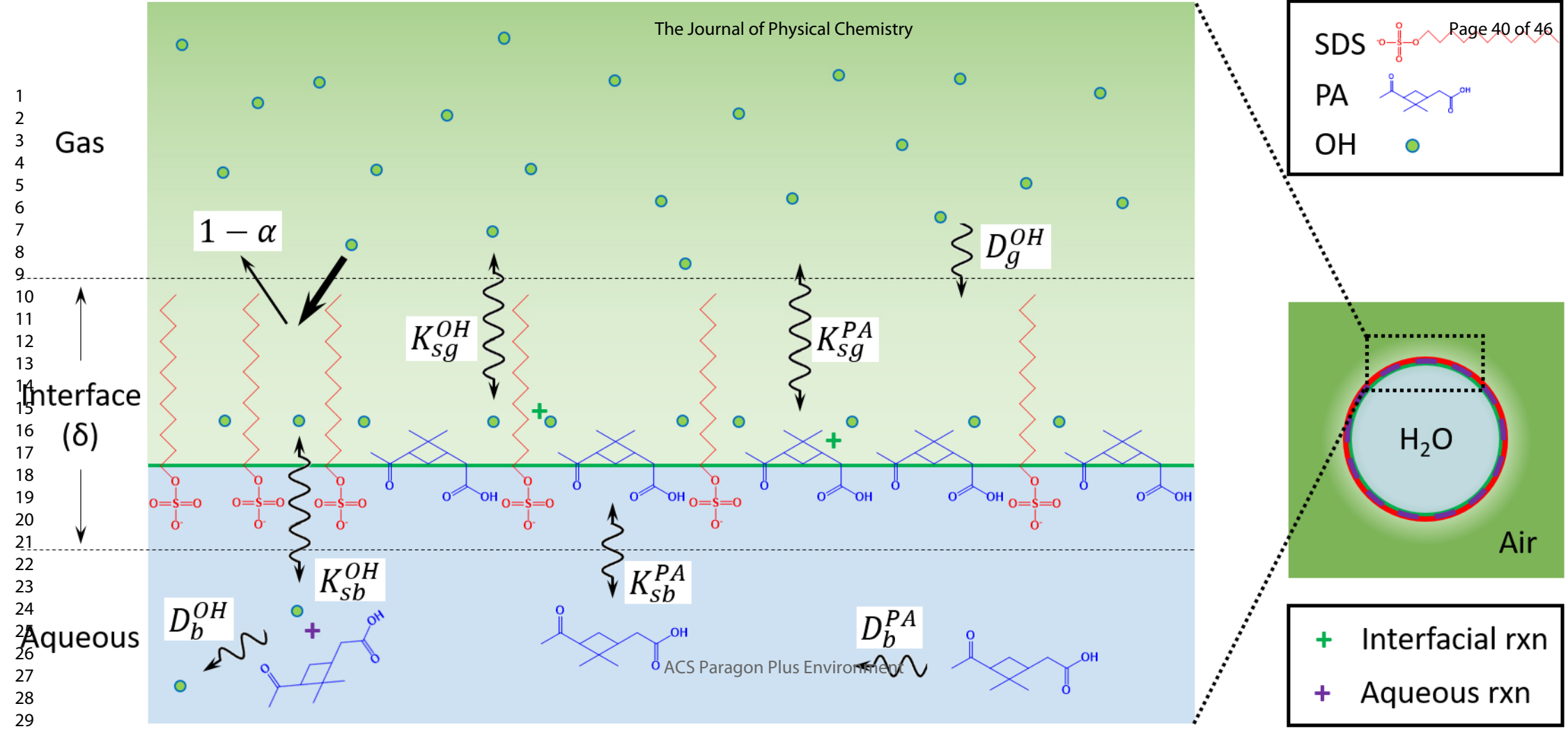
Gas
Interface
(δ)
Aqueous
$1-\alpha$
K_{sg}^{OH}
K_{sg}^{PA}
D_g^{OH}
K_{sb}^{OH}
K_{sb}^{PA}
D_b^{OH}
D_b^{PA}
SDS
PA
OH
H_2O
Air
Interfacial rxn
Aqueous rxn

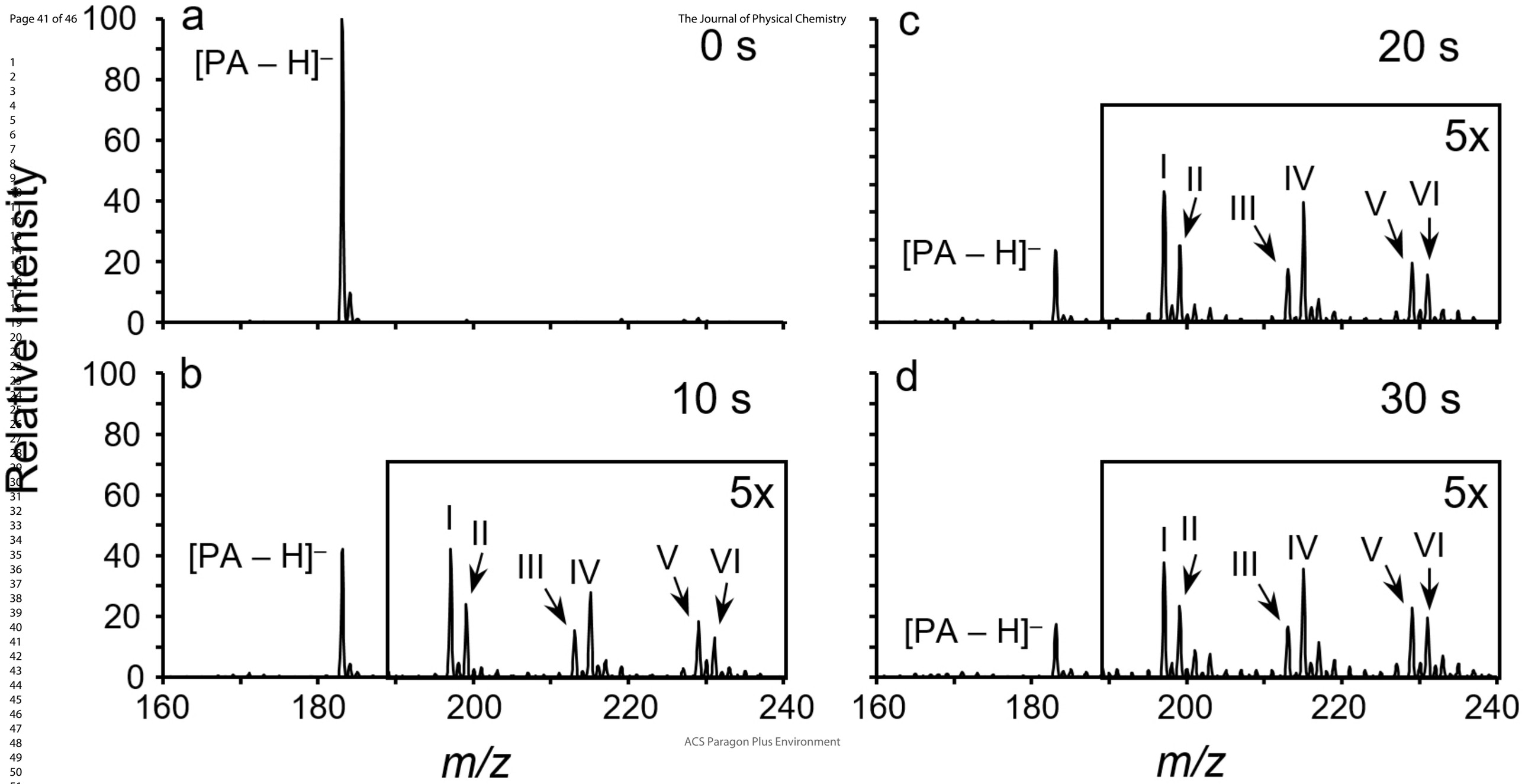
a
0 s
[PA – H]⁻
b
10 s
[PA – H]⁻
5x
I
II
III
IV
V
VI
c
20 s
[PA – H]⁻
5x
d
30 s
[PA – H]⁻
5x
Relative Intensity
m/z
m/z
0
20
40
60
80
100
160
180
200
220
240

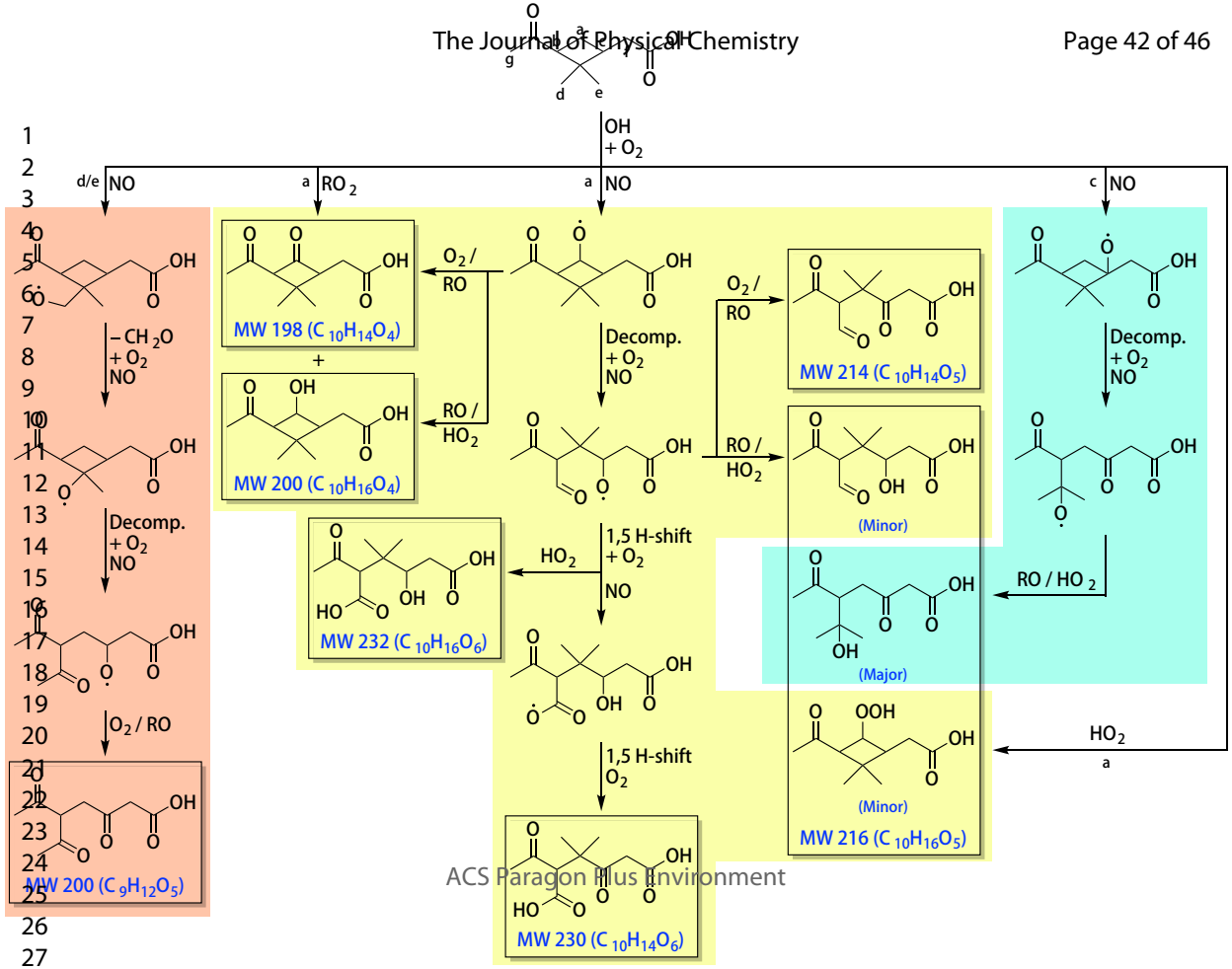

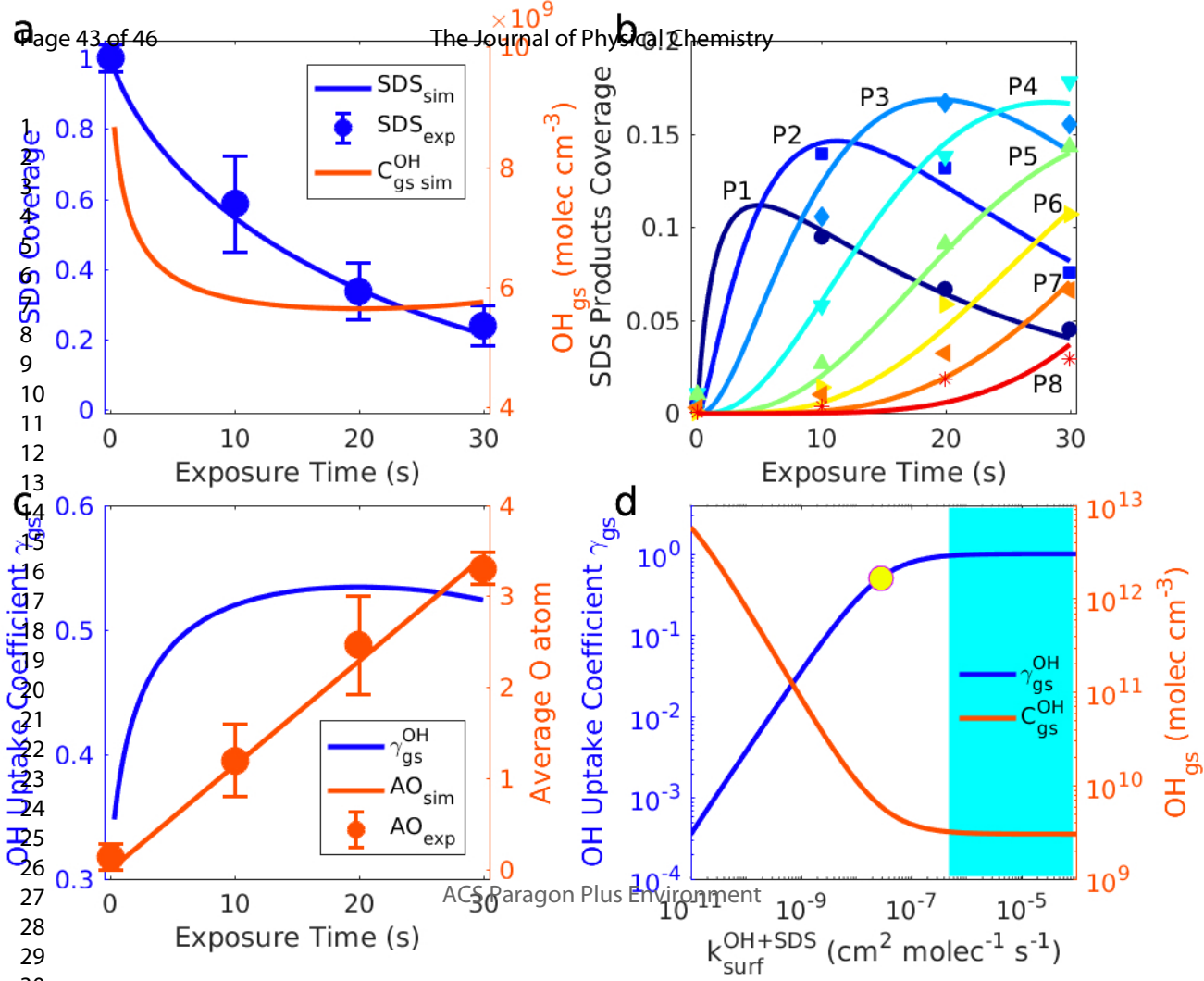

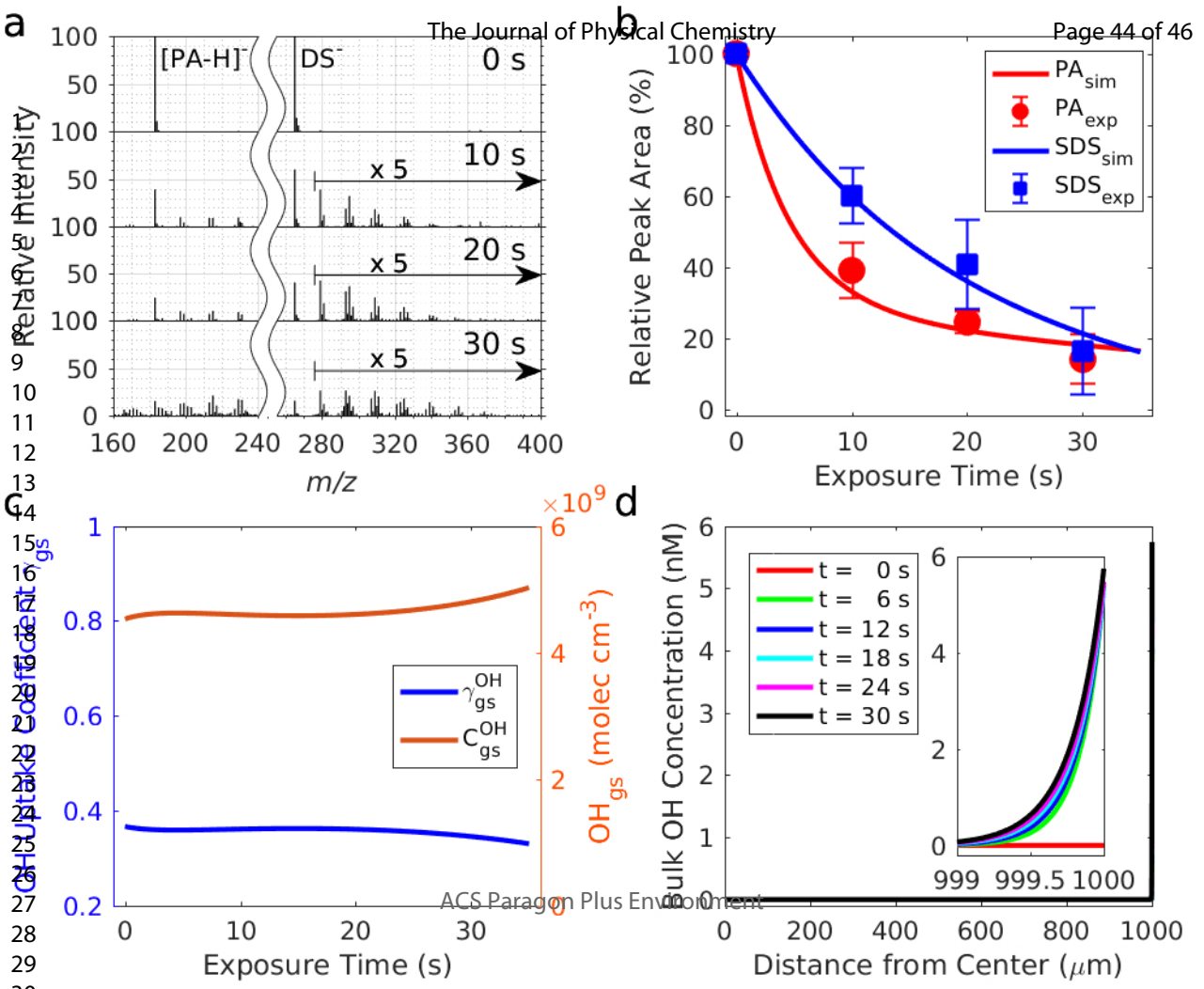

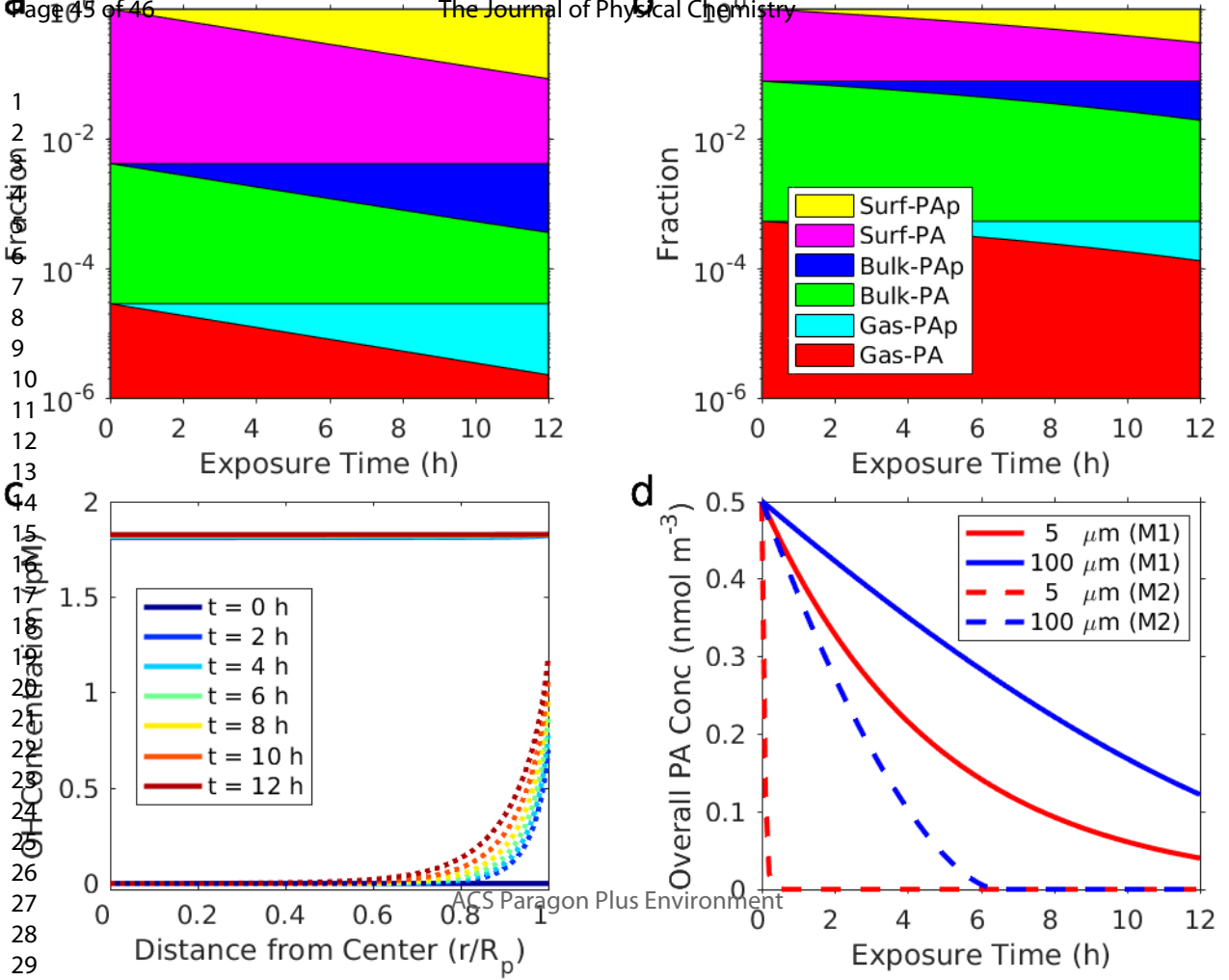
a
b
c
d
Fraction
Exposure Time (h)
Surf-PAp
Surf-PA
Bulk-PAp
Bulk-PA
Gas-PAp
Gas-PA
OH Concentration (pM)
Distance from Center (r/R_p)
t = 0 h
t = 2 h
t = 4 h
t = 6 h
t = 8 h
t = 10 h
t = 12 h
Overall PA Conc (nmol m^-3)
5 μm (M1)
100 μm (M1)
5 μm (M2)
100 μm (M2)